DOI: 10.38027/N10ICCAUA2025EN0141

Chapter 10

Predictive Routing for Airborne Monitoring of Heritage Areas

* Salvatore Polverino, Rokhsaneh Rahbarianyazd

Introduction

The principal guidance for the conservation of the environment, cities, and buildings has been meticulously developed by supranational governing bodies such as UNESCO (United Nations Educational, Scientific and Cultural Organization) and ICOMOS (International Council on Monuments and Sites) (Zaina, F. et al., 2022). These organizations serve as political barometers, with the UNESCO World Heritage Committee annually elucidating interpretations of architectural heritage conservation.

The objective and rationale of urban development significantly impact historical cities. Liang, Wen, et al. (2023) assert that mere conservation of buildings is insufficient, emphasizing the need for heritage and sustainable development to progress in tandem, as articulated in the 2011 Recommendation on the Historic Urban Landscape. This endorsement highlights contradictions between architectural heritage conservation and modern urban development, arguing that the rigid and dogmatic connotations of the 1964 Venice Charter are obsolete; from this viewpoint, history and development are seen as mutually beneficial contexts (Najd Deghati, M. et al., 2015) in the act of preserving the lexicon of urban heritage (Nia, H. A et al., 2017).

The urgency to safeguard archaeological parks and monuments in urban areas, both before and after conflicts, is evident (Barakat, S., 2021). This relevance aligns with the latest orientations from the 2005 Vienna Memorandum by UNESCO and the 2015 Recommendation for the Protection and Promotion of Museums and Collections, stressing the importance of protecting and preserving cultural heritage in museums. This includes safeguarding collections from risks such as theft, damage, degradation, and natural disasters, with a focus on advanced technological integration of digitalization.

As a consequence, the air-digital interaction was first recognized in 1954 under the canonical aspect of armed conflict, followed by the 1999 Second Protocol of the Hague Convention, which introduced enhanced protection for cultural sites of significant importance. ICCROM's Course on First Aid to Cultural Heritage in Times of Crisis trains cultural heritage professionals to provide immediate assistance to damaged cultural assets during conflicts, covering damage assessment (Chizzoniti, G. et al., 2023), site stabilization, and collaboration with local communities and humanitarian agencies. Despite these efforts, challenges arise from the qualitative exploration of Electronic Warfare (EW) and its impact on energy and monitoring systems (Leijonhufvud, Gustaf et al., 2021) delving into a functional approach of the built surroundings (Loulanski, T., 2006), e.g. for context-responsive historical landscapes (Di Mauro, L. et al., 2024) in line with its derived bunker archeology (Schofield, J., 2009) and anti-aircraft shelters (Rosser, P. et al., 2024) addressed to newfound gentrification definitions with an "allied alteration" in the built environment (Rahbarianyazd, R., 2017). Parallel to this, we acknowledge an intrinsic separation between physical heritage buildings and their social use applying economic evaluations as a correction factor of urbanism (Madrigal, J., 2018) and energy audits (Richards, J., et al., 2022) via sensor-based architecture, critical for institutional building management. Research databases notably lack information regarding conflicts involving heritage, except for physical and classical inscriptions (Borja, A., 2021), historically used to demonstrate moral victory over another civilization.

Contemporary threats involving detonations and artillery, combined with the physical confiscation of property by armies, as outlined in 10 U.S. Code § 2579 - War booty (Feis, H., 2016), highlight the shift to digital services. An

Corresponding Author: * Salvatore Polverino, Rokhsaneh Rahbarianyazd
Department of Architecture, Faculty of Engineering and Natural Sciences, Alanya University, Alanya, Türkiye
Corresponding Author's * e-mail: polverinosalvatore@outlook.com

How to Cite This Chapter:
Polverino, S., & Rahbarianyazd, R. (2025). Predictive routing for airborne monitoring of heritage areas. In Rokhsaneh Rahbarianyazd & Hourakhsh Ahmad Nia (Eds.), *Resilient Heritage & Adaptive Urbanism* (pp. 95–123). Cinius Yayınları.
https://doi.org/10.38027/N10ICCAUA2025EN0141

increase in qualitative factors, is yearly portrayed by the UNESCO Cultural World Heritage Sites (WHS) which has recently shared a boost of input variables following the definition of Outstanding Universal Value (OUV). As Roha W. Khalaf (2017) mentions, "If a World Heritage property is destroyed and later reconstructed, could it still be recognized as World Heritage?". This issue involves a signal about invisible forces in the aerial ether, with author Khalaf (2017) posing questions about the initiation, technical training, construction materials, guidelines, impact assessments, and assessment team for reconstruction.

Emerging from the EW context and cyberspace (Choi, S. et al., 2020), volatile data related to cultural, moral, and scientific supremacy emphasize the impact of military data acquisition and the display of such data as a form of spatial conquest. Subsequentially, a marginal bibliography regarding the quantitative manufacturing aspect of Unmanned Combat Aircraft System (UCAS) considers data inputs in estimation matrices.

Nonetheless, significant non-disclosure due to classification poses severe research limitations, including adversarial UAS (Unmanned Aircraft System) aeronautical data (Balcerzak, T. et al., 2022), in large part unreleased, and the hypothesis of a designated archaeological zoning buffer under EW pressure.

This hypothesis is supported by previous departmental research advocating for no-strike lists along Italian borders against foreign forces in the Mediterranean basin for battlefield key terrain models (Spennemann, D., 2020) favoring Heritage Building Information Modeling (HBIM) (Spennemann, D., et al., 2019).

Parallel to ICCROM-UNESCO Outstanding Universal Value guidelines, this research examines an advanced outlook of EW supervision, concentrating on predictive national prevention strategies, as illustrated in the Aerial view retrieved from Google Earth Imagery of Figure 1 (a).

To reinforce the paradigm, we focus on enhancing Situational Awareness (SA) for the southernmost region of Italy, specifically along the southwestern coast of Sicily, as illustrated in Figure 1 (b), an area acutely vulnerable to non-European influences; this region aims to protect identity-bound historical landmarks (Hamurcu, et al., 2020; Brosché, et al., 2016), which have been neglected during wartime, as noted by Hoeniger (2024).

Key for peacetime context evaluation, the X-47B UCAS is designed to carry various EW payloads, including jammers and Electronic Intelligence (ELINT) receivers, enhancing its operational versatility (Sozinov, A., et al., 2023), e.g. its carrier-based takeoff and landing capability makes it suitable for coastal surveillance and amphibious operations in adverse weather; given its exclusive purpose as a demonstrator, it's designated to prompt critical assessments of its cost-effectiveness and the strategic value of continued development in observance to this unmanned aerial vehicle detection category (Seidaliyeva, U. et al., 2023) and their implied anomaly (Wu, Y. et al., 2024).

In last instance, the rationale behind this study relies on the intricate protection of this settlement, as seen in Figure 2 (a), serving as an exemplary case study for EW management, emphasizing the heterogeneous land cover of the Selinunte Park and its adjacent areas, highlighted in Figure 2 (b).

This locale is characterized by a wide range of buffering zones, thereby presenting a complex and rich environment for the application of EW strategies (Chetverikov, B., Babiy, L. et al., 2024).

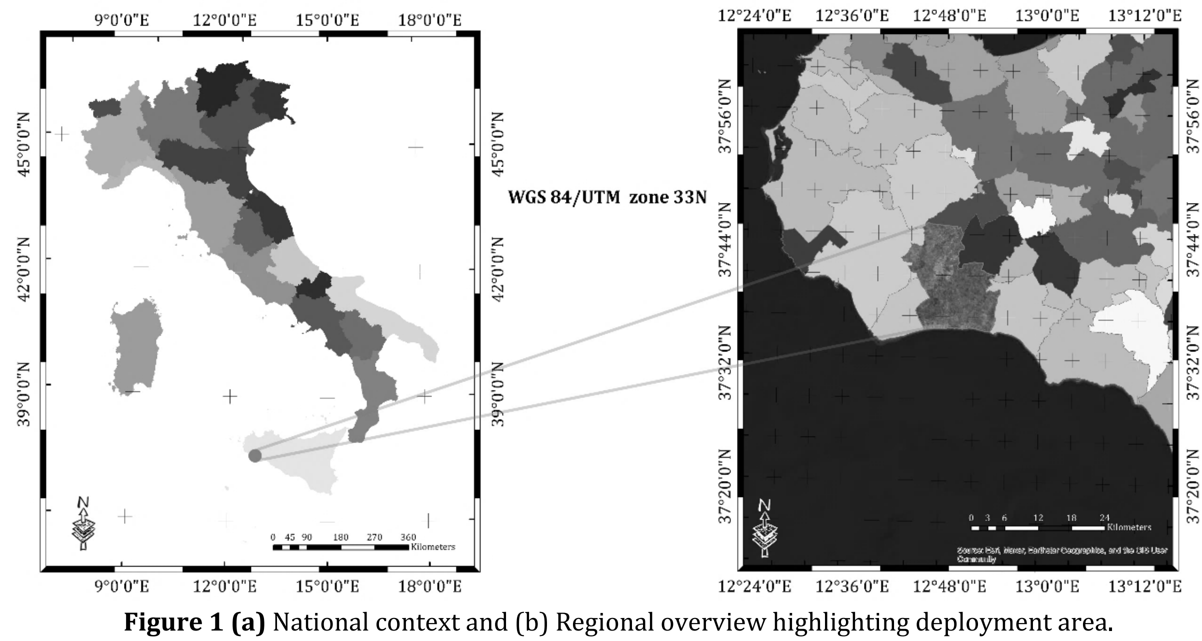

Figure 1 (a) National context and (b) Regional overview highlighting deployment area.

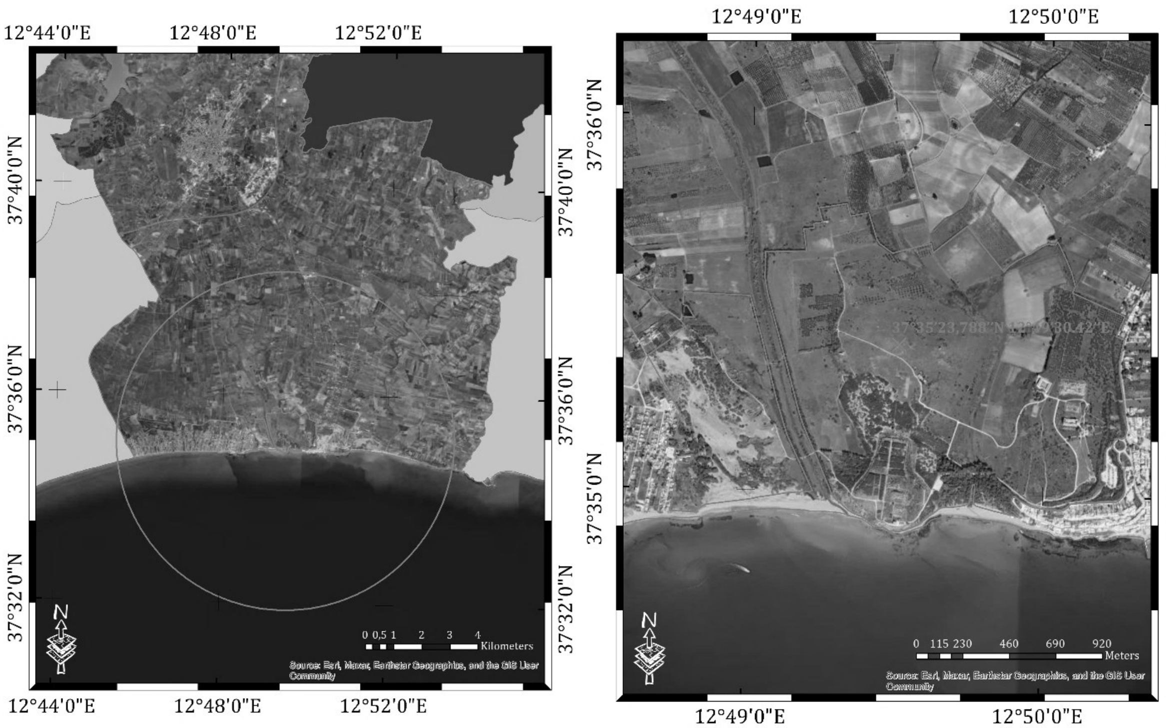

Figure 2 (a) Close-up of the operational area and **(b)** Detailed aerial view of deployment site.

1.a. Literature Review: pioneering unmanned demonstrators for carier operations

Through rigorous analysis, we select the most pertinent deployment methodologies, commenced in Figure 3, with a detailed examination of orientations to improve EW supervision and UCAS positioning.

By establishing a hierarchical decision-making framework based on three phases, the research incorporated a binary decision-making process, explicitly delineating "yes" and "no" choices to avoid regression and ensure consistent progress.

This systematic approach is divided into three essential phases: i) Preparation Phase; ii) Weighting Calculation Process, and iii) Decision-Making Appraisal Phase.

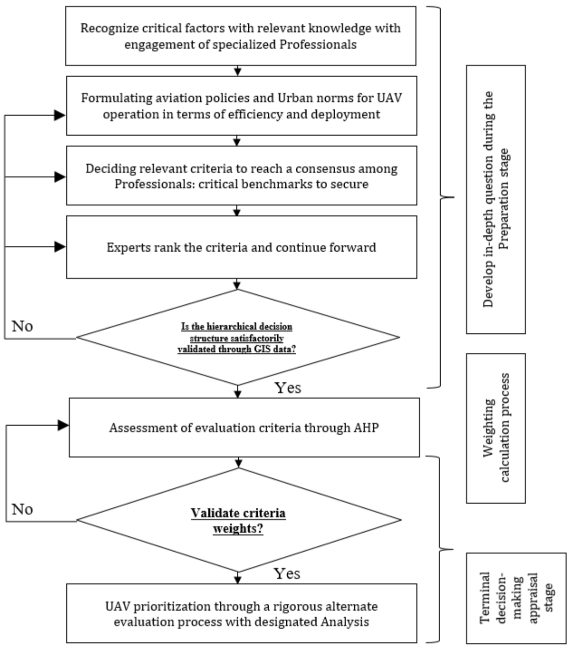

Figure 3. Hierarchical decision-making structure for UAS deployment in US Navy operations: three stages approach.

The **Preparation Phase** (Stage 1) involved framing research queries and gathering pertinent data on parameters such as 3D distance, signal intensity, interference levels, Radar Cross-Section (RCS), and jamming immunity; proven critical, this phase rated the X-47B UCAS's operational efficacy ranked on the USS George H.W. Bush (CVN-77) (Committee Air Force, 2014), including key activities such as catapult launch, recovery, emerging kinetic control techniques for hull feedback (Smith, N. et al., 2011), and wingtip folding, at peak performance with Computational Fluid Dynamics (CFD) and surrogate-based optimization (SBO), as evidenced in aerodynamic impacts and mechanical reliability (Wang, R. et al., 2022).

The **Weighting Calculation Process** (Stage 2) applied Geographic Information System (GIS) data and Multi-Criteria Decision Analysis (MCDA) to meticulously determine the relative significance of factors influencing the X-47B's operational effectiveness: accordingly, this MCDA method involved assigning exact weights to each input raster layer and summing each criterion, as statistically validated, to produce coherent and consistent output rasters.

As a result, the designated weights for the input layers were rated as follows: Hopping (1), Damage (1), Path Loss (2), Velocity (3), 3D Distance (4), No Savitsky-Golay Section 4 Unfiltered (5), and Savitsky Filter Applied (6). Each criterion was rigorously prepared and assigned its specific weight within the weighted sum tool in the ESRI® environment, ensuring exceptional levels of consistency and accuracy.

Within the scope of kernel trajectory analysis, the criterion with the Savitsky filter applied shows a subtle but significant influence, owing to its nuanced impact on the comprehensive analytical framework.

The **Decision-Making Appraisal Phase** (Stage 3) employed the Cramer-Rao Lower Bound (CRLB) and exponential smoothing to improve the accuracy and reliability of radar spatial data in detection probability (Yuan, C. et al., 2024). Defuzzification and consistent monitoring ensure data readiness and accuracy.

Steadily within this assessment framework, the iterated series of trajectories achieved high consistency, and unbiased estimators verified all criteria layers making comparisons with the 3D spatial representation of radar data visualising signal variations at critical points, refining error bounds through CRLB and exponential smoothing, random variability and enhanced measurement clarity in elevation angles, azimuth, and signal strength.

1.b. A three-stage preliminary context: objective from the Literature Review emerged

Making comparisons for predictive modelling during peacetime (Stone, P., 2022), Situational Awareness for ground systems, has incorporated laser-scanned data, InSAR, and rigorous GIS procedures for archaeological-historical site mapping (Bozzano, M. et al., 2024; Chetverikov, B., Hlotov, V., et al., 2024), also analyzing decibel Path Loss signals and morphological attributes extracted from the 10-meter resolution Digital Elevation Model (Tarquini, S. et al., 2017), vegetation health, and subsidence.

Contradicting the assumption that advanced technological systems are universally applicable for heritage site protection, the high cost and complexity of these advanced systems may limit their practical application in many heritage sites, particularly those in resource-limited settings. The adaptation of military-grade technology to civilian contexts may require significant modifications, introducing new vulnerabilities or operational challenges.

As evidenced by the archaeological zoning of Fire trenches in Bükk National Park (Hungary), the demonstration of advanced geospatial techniques indicates significant potential, albeit their practical implementation for EW protection remains uncertain (Juhász et al., 2016).

Notably, a noticeable trend has emerged in terms of countermeasure effectiveness, which is vital for sensor systems detecting real-time variable factors, as implied by Wu et al. (2024) and Zhang et al. (2022) by the same token for these anomalies, considered peacetime disruptors.

Lastly, and ancillary to the MCDA three-stage scope, the featuring of a 3D Active Electronically Scanned Array (AESA) subject to Electronic Attack (EA), e.g. frequency hopping and jamming resistance, has included morphological data operated by the Saab Giraffe 4A Radar System; the evaluation, albeit limited due to the focus on overall avionics trends and computational tests for Selinunte area park and designated as iterative research by the Department, employs multiple MCDA techniques to optimize the system.

1.b.I. Stage 1: overcoming static weighting assumptions in military operations

While these methodologies aim to enhance protection against EW threats, their alignment with the practical needs and resources of heritage site management remains a critical consideration.

In reverse, unlike the narrow focus of UCAVs, the UCAS system exemplifies a broader, more integrated network. By combining combat vehicles with advanced command and communication systems, UCAS offers a more comprehensive and adaptable operational framework.

The Weighting Calculation Process, integrating GIS in MCDA, aimed to enhance the X-47B's operational effectiveness but introduced rigidity by overlooking the dynamic nature of real-world environments. This inflexibility could lead to suboptimal decisions, as the process assumes weights remain constant under all conditions. To counter this, the Savitsky-Golay filter was incorporated, providing a more flexible, adaptive approach to weighting (Selver, M. et al., 2018).

1.b.I.a Range estimation refinement in MCDA key criteria framework

To better contextualize the three-stage decision-making pipeline, integrating Command & Control airworthiness data from the electronic Consolidated Automated Support System (eCASS) highlights the necessity of incorporating the technological behaviour of AESA radar. By integrating the eCASS protocol, the Systems-Theoretic Process Analysis (STPA) aids in identifying potential hazards and mitigating risks in correspondence with the critical points.

The MCDA framework synergizes with STPA actions to detect critical points for UCAS operations, ensuring safety and reliability by analyzing potential failures and dangerous interactions. As visualized in Figure 4, key elements from the framework provide sequentially a detailed model of the control structure:

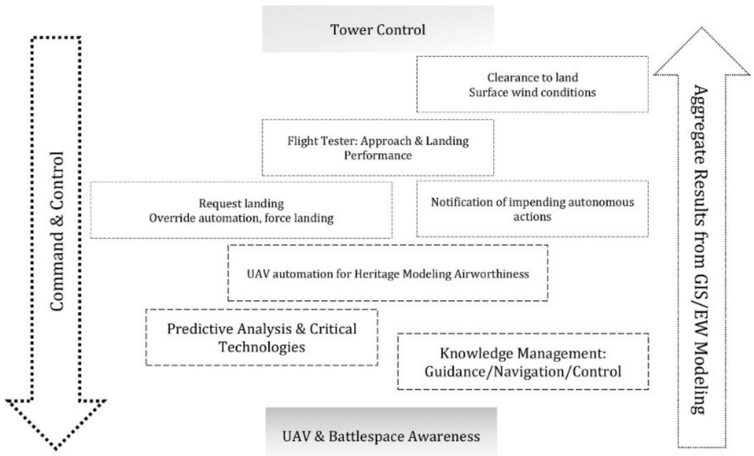

Figure 4. Applying MCDA methodologies to identify Key Criteria: eCASS and STPA.

The first stage involves Command & Control, which ensures that UCAS operations are effectively managed and coordinated. This includes Predictive Analysis & Critical Technologies, where data-driven insights and advanced technologies are used to anticipate and address potential issues. Knowledge Management encompasses Guidance/Navigation/Control, ensuring that all relevant information is accurately disseminated and utilized for optimal decision-making.

In the second stage, UCAS Automation for Heritage Modeling Airworthiness is crucial for maintaining operational safety and compliance with regulatory standards. This phase also includes Request Landing procedures, where automation can be overridden for forced landings if necessary. Flight Tester operations focus on Approach & Landing Performance, ensuring that UCAS lands safely under various conditions.

The third stage addresses the final clearance and notifications. Clearance to Land involves assessing surface wind conditions to ensure safe landing operations. Notification of Impending Autonomous Actions ensures that all relevant parties are aware of the UCAS's autonomous operations and any potential changes.

Throughout these phases, aggregate results from GIS/EW Modeling provide essential data and insights that inform and enhance the overall decision-making process.

1.b.II. Stage 2: research question aimed at the integration of input variables

To trigger the **Weighting Calculation Process**, a qualitative selection of appropriate technologies required careful consideration addressing the question: "How can multi-criteria decision analysis (MCDA) techniques can be translated in terms of mathematical information in terms of EW countermeasures for protecting cultural heritage sites?".

Subsequently, albeit not incorporated within the computational matrixes, as technologically incorporated in the UCAS system, the AESA radar participates in resource allocation via digital transmit/receive (T/R) modules with 360° scan coverage and data handling pipelines (Park, J. et al., 2021).

Visually, the sophisticated Digital Signal Processing (DSP) algorithms, including Fast Fourier Transform (FFT) and adaptive filtering, support the seamless operation of the UAS/UCAS in complex and contested environments, simultaneously, as clarified in Figure 5, with the highest rates of information processing; this underscores the clear need for scalable models.

Correspondingly, the **Decision-Making Appraisal Phase** aided the robustness of these systems in real-time data fusion and adaptive responses critically assessed by assigning input variables following the Consolidated

Automated Support System (eCASS) the Systems-Theoretic Process Analysis (STPA) by Rising, J., and Leveson N. (2018); in comparison, the Saab Giraffe 4A was noted for its ability to detect UCAS threats, notwithstanding limited to a specific frequency band.

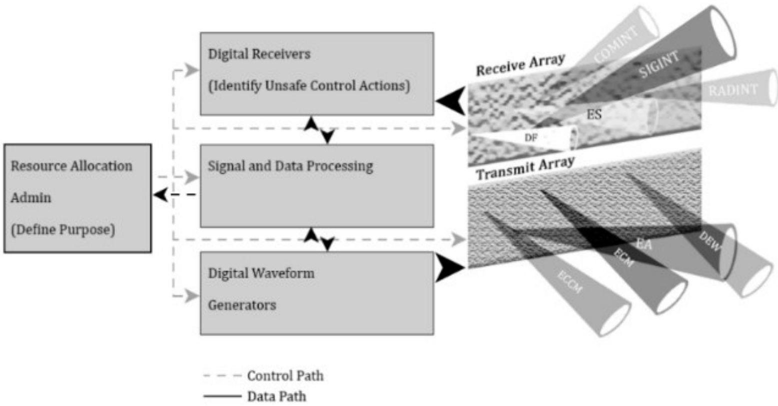

Figure 5. Conceptual framework Architecture of AESA. Inputs and Outputs.

1.b.II.a. Research question aimed at the integration of input variables

To benchmark this initial set, the review evaluated the effectiveness of various MCDA methods, embracing theoretical models by Zhang, and enhancing the Saab Giraffe 4A Radar System's performance in safeguarding cultural heritage sites from EW threats. Key features (A) include the Giraffe Radar System's feature matrix $\boldsymbol{g_{ij}}$, representing specific capabilities or performance measures of the designated UCAS trajectory.

$$\boldsymbol{G} = \begin{bmatrix} g_{11} & g_{12} & g_{13} & g_{14} & g_{15} \\ g_{21} & g_{22} & g_{23} & g_{24} & g_{25} \\ g_{31} & g_{32} & g_{33} & g_{34} & g_{35} \end{bmatrix}$$

(A). The matrix of input variables is organized column-wise from left to right and includes: i) 3D AESA Technology; ii) Frequency Hopping; iii) Advanced Algorithms; iv) Signal Processing and v) Interference Mitigation.

i) 3D AESA Technology $(\boldsymbol{g_{11}})$ which provides enhanced detection and tracking of multiple targets with high accuracy and resolution exemplified by the following Volume integral:
$$g_{11} = \int_{x_1}^{x_2}\int_{y_1}^{y_2}\int_{z_1}^{z2}\left(\frac{\partial^2 f}{\partial x^2}+\frac{\partial^2 f}{\partial y^2}+\frac{\partial^2 f}{\partial z^2}\right)dx\,dy\,dz \text{ ; } \textbf{(A.a)}$$

ii) Frequency Hopping $(\boldsymbol{g_{12}})$ which utilizes rapid changes in frequency to avoid detection and interception by adversarial jamming systems: $g_{12} = \sum_{i=1}^{n} f_i(t) \cdot \text{hop}\,(t_i)$; **(A.b)**

iii) Advanced algorithms $(\boldsymbol{g_{13}})$ which incorporates algorithms to detect and counteract various forms of electronic interference: $g_{13} = FFT\left(\frac{1}{T}\int_0^T x\,(t)e^{-j2\pi ft}dt\right)$; **(A.c)**

iv) Signal processing $(\boldsymbol{g_{14}})$ which uses robust signal processing techniques to filter out noise and maintain clear communication channels: $g_{14} = \mathbf{H}\,(s) = \frac{N\,(s)}{D\,(s)}$; **(A.d)**

v) Interference Mitigation $(\boldsymbol{g_{15}})$ which actively identifies and mitigates interference from both intentional jammers and environmental noise: $g_{15} = \max_k\left(\frac{\mathrm{I}_k}{\mathrm{J}_k}\right)$; **(A.e)**

1.b.III. Stage 3: Counter-Measure robust estimation

The adaptiveness of EW operations in estimating target range using Fast Fourier Transform (FFT) is considered in fault models (Zou, Y. et al., 2024). For each FID, the ground system computes variables from raw data, detailing the signal, including noise and transient spikes within the first UCAS sector, at a frequency of 0.18 GHz, ranging within 6.82 ± 5.84.

Complementary to this, noise figure (NF) further layers of Counter-Measures, e.g., Man-in-The-Middle (MITM) and Denial-of-Service (DoS) (Liang, X., 2017) at the expenses of IoT-based battlefield units (Kovschavov, A. A., 2019), adopt transversely range estimation calculation (Ling, Q. et al., 2023) and noise level in the receiver.

Equation B also confirms the received signal S_i at frequency f_r:

$$S_i\,(f_r) = A_i\, a_r \left(\frac{f_r}{B}\right) exp\left(-j\,\pi \frac{f_r^2}{\gamma}\right) exp\left(-j\,2\pi\, f_r \frac{2R_i}{c}\right);$$ **Equation B (**Ling, Q. et al., 2023**).**

To calculate the range R_i to the target, with c, speed of light and t_i, the time delayed of the received signal, as shown in Equation C:

$$R_i = \frac{c \cdot t_i}{2};$$ **Equation C (**Ling, Q. et al., 2023**).**

To establish the upper and lower bounds of the range estimation, we evaluate the components 6.82 and 5.84, derived from the frequency bandwidth and other system parameters, as evidenced in Equation C.a and C.b:

$$R_{upper} = \frac{c \cdot (6.82 + 5.84)}{2} = 1.899 \times 10^9 \text{ m};\; R_{lower} = \frac{c \cdot (6.82 - 5.84)}{2} = 1.47 \times 10^8 \text{ m};$$

Equations C.a, C.b.

In accordance with the previous equations, we calculate the SINR, as a measure of signal quality, tailored to two Weighted versions: i) W. Signal Strength, as Strength of the received signal and ii) W. Noise Level, as Level of noise in the received signal, as outlined in Equation D:

$$\text{SINR}_{\text{weighted}} = \frac{(\text{Weighted Signal Strenght})^2}{(\text{Weighted Signal Strenght})^2 + 2 \times (\text{Weighted Noise Level})^2};$$ **Equation D.**

To reinforce this monitoring aspect, we assume a robust and effective Fisher information, as presented in Equation E, to realistically accommodate our set of observation, and accommodate: R (range), θ_{el} (elevation angle), θ_{azi} (azimuth angle), A (amplitude) and N (noise); subscripts in the elements, such as $I_{R,\theta_{el}}$, $I_{A,\theta_{azi}}$, a relationship of covariance between the parameters is expressed:

$$\mathbf{I}(\theta) = \begin{pmatrix} I_R & I_{R,\theta_{el}} & I_{R,\theta_{azi}} & I_{R,A} & I_{R,N} \\ I_{\theta_{el},R} & I_{\theta_{el}} & I_{\theta_{el},\theta_{azi}} & I_{\theta_{el},A} & I_{\theta_{el},N} \\ I_{\theta_{azi},R} & I_{\theta_{azi},\theta_{el}} & I_{\theta_{azi}} & I_{\theta_{azi},A} & I_{\theta_{azi},N} \\ I_{A,R} & I_{\theta_A,\theta_{el}} & I_{A,\theta_{azi}} & I_A & I_{A,N} \\ I_{N,R} & I_{N,\theta_{el}} & I_{N,\theta_{azi}} & I_{N,A} & I_N \end{pmatrix};$$

Equation E. Fisher Matrix.

$$I_R = \frac{2 \cdot \text{SNR} \cdot \text{B} \cdot T^2}{c^2} \quad \text{a)}$$

$$I_A = \frac{2 \cdot \text{SNR}}{c^2} \quad \text{b)}$$

$$\text{NF} = 10 \log\left(\frac{SNR_{in}}{SNR_{out}}\right) dB \quad \text{c)}$$

Equations E. a) b) c).

1.c.I. Scrutinizing eCASS: Key Factors in UCAS Performance

As indicated for the component 3D AESA Technology **(g_{11})**, issues related to incorrect maintenance and aggregate results are critical. Contrasting to this incoherent raw data intercepted highlighted in Figure 6, we consider the disaggregation from the smoothing process targeting the first sector (Sector 1_V, highlighted in light green) utilizing Savitsky-Golay filtering, HRBFN_Output, and MP Output, spanning within the interval 6.82 ± 5.84.

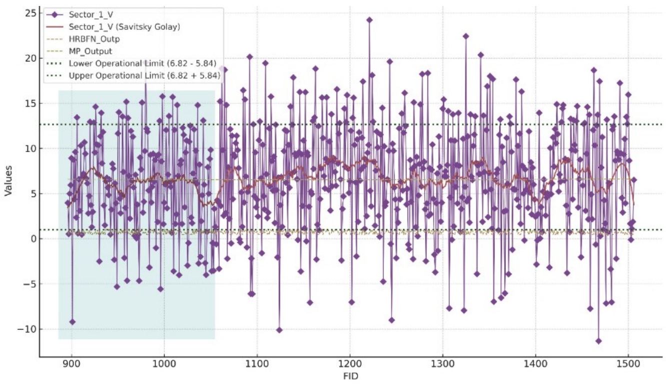

Figure 6. Detailed sector-by-sector monitoring of Savitzky-Golay Filter Performance Across All X-47B UCAS Sectors.

By the same token, the efficacy of the HRBFN (Heterogeneous Radial Basis Function Network), is highlighted, embracing a neural network model optimized for nonlinear function approximation and large dataset processing, integrating GHz frequency data, FID (Feature Importance Determination), and damage intensity metrics to deliver a comprehensive assessment of EW impacts on X-47B operations. On the other hand, the MP (Matching Pursuit) algorithm facilitates sparse signal representation, enhancing the robustness of data analysis in complex operational environments.

Nonetheless, this early critical assessment reveals potential pitfalls; in instance, the accuracy of the HRBFN model in real-time scenarios is crucial as we consider that the integration of GHz frequency data with FID and damage intensity metrics, while comprehensive, may encounter challenges related to data synchronization and processing speed.

Additionally, the MP algorithm's performance in sparse signal representation should be evaluated for potential limitations in handling high-noise environments and rapidly changing signal dynamics.

As evidenced in Figure 7, the comparative monitoring underscores the Savitsky Golay filter's capability to maintain signal integrity and operational reliability within sector 1 of the X-47B (EW features selection highlighted in light green) $f(t) = f_c + k_f \cdot m(t)$ (Proakis, J. and Salehi, M., 2007):

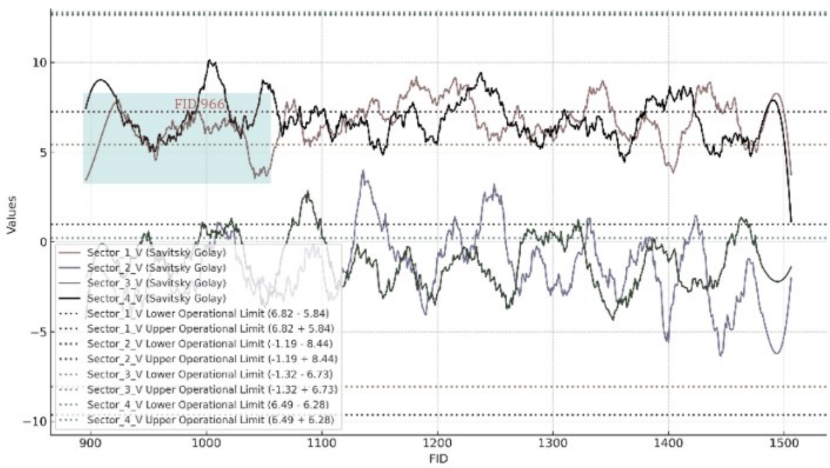

Figure 7. Savitsky Golay enhanced for Sector 1.

2. Materials and Methods

The materials derive from the corresponding manuals in terms of data, progressively simulated using advanced Python modelling modules such as NumPy, SciPy, Matplotlib, SimPy, PyDSTool, and TensorFlow, thus, selected for their capabilities in handling complex numerical operations, scientific computing, data visualization, discrete-event simulation, dynamical systems analysis, and machine learning, respectively including 3D active electronically scanned array (AESA), frequency hopping and section radar (Sijabat, P. et al., 2021), and sophisticated jamming resistance whose datasets are compatible with AHP-related models (Alharasees, O. et al., 2024, Chang, Da-Yong, 1996).

In the last instance, the computation allowed limited space for a Proximal Policy Optimization (PPO) algorithm (Ran, W. Et al., 2023) backed up by AESA thermal factors; this vision algorithms X-47B variables' allocation (Kong, X. et al., 2023, Belal A. et al., 2019) is benchmarked according to FID critical points across Path Loss GIS information in Selinunte area park, retrieved from previous departmental research (Polverino, S., 2024), thus strengthening its standing and authority internationally as an Institutional Chamber of Architects. This positions the department to play an active role in the transformation and defence of the historical Italian landscape in cooperation with the defence industry.

2.a. eCASS decision matrix

Fuzzy AHP handles distinctively uncertainty using fuzzy pairwise comparison matrices (Chen, Chen-Tung et al., 2006), computing fuzzy synthetic extent values, defuzzifying, normalizing weights, and calculating scores (Zadeh, A., 1965). BWM focuses on the most and least important criteria applied in stochastic MCDA models (Mohammadi, M. et al., 2020), solving an optimization problem to calculate composite scores. ELECTRE compares alternatives by constructing a decision matrix, assigning weights, calculating concordance and discordance indices, and ranking alternatives.

ANP extends AHP by considering interdependencies (Taherdoost, H. et al., 2023), forming and normalizing a supermatrix, and deriving composite scores from the limit supermatrix. Data for criteria like 3D Distance, Frequency Hopping (2-4 GHz), Signal Strength (40-100 dB), Interference Level (0-50 dB), Radar Cross-Section (0.01-10 m^2), and Jamming Resistance (0-1) were normalized and analyzed using these MCDA methods. For example, a scenario with values D = 3090.88 meters, F = 3.0976 GHz, S = 85.92 dB, I = 16.68 dB, RCS = 3.73 m^2, and JR = 0.2244 yielded a composite damage score of 0.6683 using AHP.

3. Results overview of proposed frameworks

The tracking strategy proposed by Kennedy (2020, 2023) incorporates noise patterns also identified by Zhang et al. (2022), raw data, and Savitzky-Golay filtered values, enhanced in Figure 8. Specifically, statistical considerations from the resulting radar cross-section (RCS) data are statistically illustrated in Figure 9: most deviations are close to zero, with a minimum deviation of -7.21 m^2 and a maximum of 6.14 m^2; in response, these preliminary results demonstrate that the Savitzky-Golay filter effectively smooths the original RCS data, preserving the primary structure while reducing noise.

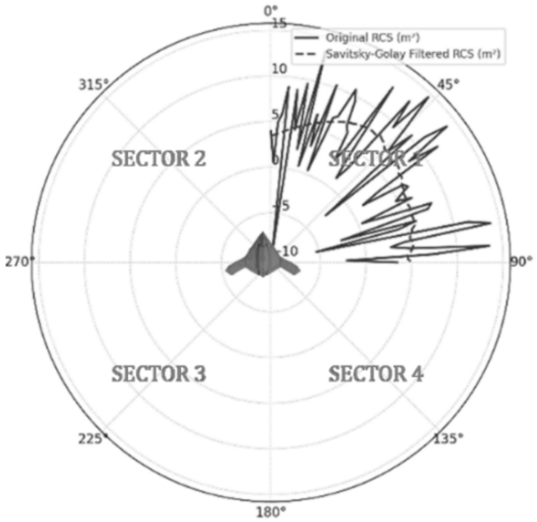

Figure 8. Radar Cross-Section. From a full 360-degree view, roughly a 1/4 section radar plot.

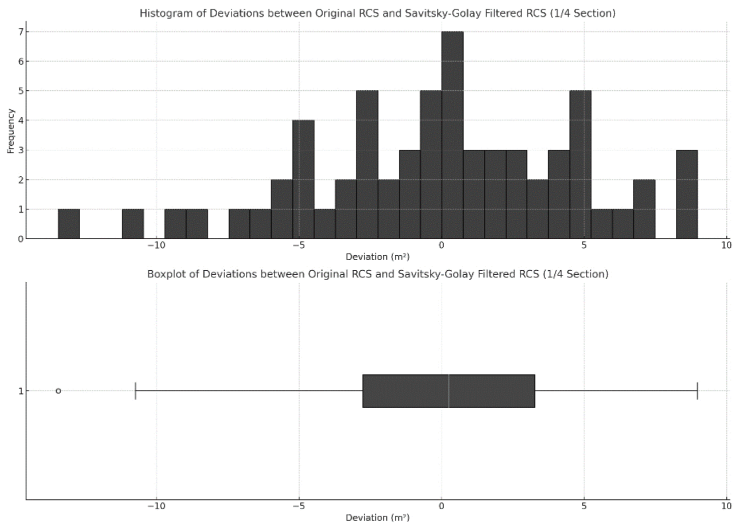

Figure 9. Mean deviation of -0.88 m^2 and a standard deviation of 3.03 m^2.

By evaluating the Radar Cross-Section (RCS) values for each measurement and analyzing the performance of three radar systems (*FID* 896, *FID* 966, *FID* 1056), the goal was to select the best radar system trajectory. This punctual assessment, based on the doctrine of critical points, involved detailed comparisons of 3D Distance, Frequency Hopping, Interference, RCS and Signal Strength, expressed in Table 1, ultimately determining the most suitable radar system for preserving the integrity of heritage sites against EW threats, concluding with a Technique for Order Preference by Similarity to Ideal Solution' (TOPSIS) evaluation, applied to select, sort, classify or label alternatives for sorties (De Souza, L. et al., 2018) to determine oppositional aspects of the methods as indicated in Table 2:

Table 1. Sampled extracted information from the X-47B telemetry via Haversine formula, including critical points.

Critical Point	3D distance [mt]	Frequency Hopping [GHz]	Signal Strength (S) [dB]	Interference (I) [dB]	RCS [m2]	JR
FID 896	3090.88	3.0976	85.92	16.68	3.73	0.2244
FID 966	4120.56	2.8765	75.34	12.45	4.12	0.3345
FID 1056	2950.34	3.1234	88.45	20.56	2.56	0.1234

Table 2. Dichotomous overview of methods including: AHP, ANP, TFN, BWM, ELECTRE, and TOPSIS.

Method	3D distance [mt]	Frequency Hopping [GHz]	Signal Strength (S) [dB]	Interference (I) [dB]	RCS [m2]	JR
AHP	Y	Y	Y	N	N	N
ANP	Y	Y	Y	Y	Y	Y
TFN	Y	Y	Y	N	N	N
BWM	Y	Y	Y	N	N	N
ELECTRE	Y	Y	Y	Y	Y	Y
TOPSIS	Y	Y	Y	Y	Y	Y

.

3.a. Results from the Multi-MCDA evaluation

AHP methodology initiated the research so that for each criterion (C_1 - 3D Distance, C_2 - Frequency Hopping, C_3 - Signal Strength), pairwise comparisons of the alternatives (*FID* 896, *FID* 966, *FID* 1056) are conducted to form comparison matrices, which were then used to derive the priority vectors for evaluating the relative importance of each alternative with respect to the given criteria as exhibited from Equations 1-6:

$$A_C = \begin{bmatrix} 1 & 3 & 0.5 \\ 0.33 & 1 & 0.25 \\ 2 & 4 & 1 \end{bmatrix}$$; **Equation 1.** $$CR = \frac{CI}{RI}$$; **Equation 2.** $$CI = \frac{\lambda_{max} - n}{n-1}$$; **Equation. 3.**

$$A_{C1} = \begin{bmatrix} 1 & 0.75 & 1.1 \\ 1.33 & 1 & 1.5 \\ 0.91 & 0.67 & 1 \end{bmatrix}$$; **Equation 4.** $$A_{C2} = \begin{bmatrix} 1 & 1.1 & 0.95 \\ 0.91 & 1 & 0.87 \\ 1.05 & 1.15 & 1 \end{bmatrix}$$; **Equation 5.** $$A_{C3} = \begin{bmatrix} 1 & 0.85 & 1.2 \\ 1.18 & 1 & 1.35 \\ 0.83 & 0.74 & 1 \end{bmatrix}$$; **Equation 6.**

In matrix form, this can be represented as: $S = W_C \cdot [W_{C1}\ W_{C2}\ W_{C3}]$ is the vector of overall scores for the alternatives whereby W_{Cj} is the weight of criterion C_j, as proved in Equations 7-10.

$$W_C = \begin{bmatrix} 0.553 \\ 0.189 \\ 0.258 \end{bmatrix}$$; **Equation 7.** $$W_{A1} = \begin{bmatrix} 0.31 \\ 0.43 \\ 0.26 \end{bmatrix}$$; **Equation 8.** $$W_{A2} = \begin{bmatrix} 0.34 \\ 0.32 \\ 0.34 \end{bmatrix}$$; **Equation 9.** $$W_{A3} = \begin{bmatrix} 0.28 \\ 0.39 \\ 0.33 \end{bmatrix}$$; **Equation 10.**

The best overall score $S(A_i) = \sum_{j=1}^{n} w_{C_j} \cdot w_{A\ i}^{C_j}$ for alternative A_2 is calculated as 0.3892 (*FID* 966) while $S(A_1)$ (*FID* 895) and $S(A_3)$ (*FID* 1056) are separately 0.3293 and 0.2815.

A second method, ANP, initially involves structuring the decision problem as a network of clusters refined through a pairwise comparison (Equation 11): for each pairwise matrix, the priority vector is solved through the normalization of each eigenvector (Equation 12); given the priority weights from λ_{max}, each comprises elements that are interrelated, for instance, in evaluating radar systems (A_1, A_2, A_3) based on criteria such as 3D Distance (C_1), Frequency Hopping (C_2), and Signal Strength (C_3), the organization is subdivided into two clusters: Criteria and Alternatives, as substantiated by Equations 11-13:

$$A = \begin{bmatrix} a_{11} & a_{12} & \cdots & a_{1n} \\ a_{21} & a_{22} & \cdots & a_{2n} \\ \vdots & \vdots & \ddots & \vdots \\ a_{n1} & a_{n2} & \cdots & a_{nn} \end{bmatrix}$$; **Equation 11.** $$A = \lambda_{max} w$$; **Equation 12.** $$W = \begin{bmatrix} W_{11} & W_{12} & \cdots & W_{1m} \\ W_{21} & W_{22} & \cdots & W_{2m} \\ \vdots & \vdots & \ddots & \vdots \\ W_{m1} & W_{m2} & \cdots & W_{mm} \end{bmatrix}$$; **Equation 13.**

Within each cluster and between clusters, pairwise comparisons are gauged to hold relative importance: these comparisons are quantified using a ratio scale, typically ranging from 1 (equal importance) to 9 (extreme importance); the resulting pairwise comparison matrices A are structured such that each element a_{ij} represents the relative importance of element i over element j as for pairwise comparison matrix enhanced within the criteria cluster (Equations 14-16), i.e. for 3D distance (C_1), A_{A1}, Frequency Hopping (C_2), A_{A2}, Signal Strength (C_3), A_{A3}:

$$A_c = \begin{bmatrix} 1 & 3 & 0.5 \\ 0.33 & 1 & 0.25 \\ 2 & 4 & 1 \end{bmatrix}$$; **Equation 14.**

$$A^*_{A1} = \begin{bmatrix} 1 & 0.75 & 1.1 \\ 1.33 & 1 & 1.5 \\ 0.91 & 0.67 & 1 \end{bmatrix}$$; **Equation 15.**

$$A^*_{A2} = \begin{bmatrix} 1 & 1.1 & 0.95 \\ 0.91 & 1 & 0.87 \\ 1.05 & 1.15 & 1 \end{bmatrix}$$; **Equation 16.**

By normalizing W_C to obtain the priority weights for the criteria (corroborated in Equation 18), similarly, priority vectors from $A^*_C\ W = \lambda_{max}\ w$, for the alternative matrices are computed (proven in Equations 17-21).

$$A^*_{A3} = \begin{bmatrix} 1 & 0.85 & 1.2 \\ 1.18 & 1 & 1.35 \\ 0.83 & 0.74 & 1 \end{bmatrix}$$; **Equation 17.**

$$W_C = \begin{bmatrix} 0.553 \\ 0.189 \\ 0.258 \end{bmatrix}$$; **Equation 18.**

$$W_{A1} = \begin{bmatrix} 0.31 \\ 0.43 \\ 0.26 \end{bmatrix} a) \quad W_{A2} = \begin{bmatrix} 0.34 \\ 0.32 \\ 0.34 \end{bmatrix} b) \quad W_{A1} = \begin{bmatrix} 0.28 \\ 0.39 \\ 0.33 \end{bmatrix} c)$$

$$W = \begin{bmatrix} W_{CC} & W_{CA} \\ W_{AC} & W_{AA} \end{bmatrix}$$; **Equation 19.**

$$W_{CC} = \begin{bmatrix} 0.553 & 0.189 & 0.258 \\ 0.189 & 0.189 & 0.258 \\ 0.258 & 0.189 & 0.258 \end{bmatrix}$$; **Equation 20.**

$$W_{CA} = \begin{bmatrix} 0.31 & 0.43 & 0.26 \\ 0.34 & 0.32 & 0.34 \\ 0.28 & 0.39 & 0.33 \end{bmatrix}$$; **Equation 21.**

The last step regarded the extraction of the weights for the alternatives from the limit supermatrix $W_\infty = \lim_{k\to\infty} W^k$ beforehand the conclusion with priority weights $w_\infty = [0.35 \quad 0.33 \quad 0.32]$. ANP method suggests that *FID* 896 (0.35) is the most preferred alternative, 966 (0.33) is the second preferred alternative while 1056 (0.32) is the least preferred alternative.

A third following method, fuzzy comparison matrices, uses linguistic terms converted (Zadeh, A. (1994) to triangular fuzzy numbers (TFN) $\tilde{A}$ = *(l, m, u)* (Sun, C., 2010) and ranked *FID* 896 (0.6683), *FID* 966 (0.6431), *FID* 1056 (0.6665), as substantiated in Equations 22-24 and framed in Table 3:

$$\tilde{S}_i = \left(\sum_{j=1}^{n} \tilde{a}_{ij}\right) \cdot \left(\sum_{i=1}^{n}\sum_{j=1}^{n} \tilde{a}_{ij}\right)^{-}$$; **Equation 22.**

$$A = \frac{l+m+u}{3}$$; **Equation 23.**

$$w_i = \frac{A_i}{\sum_{i=1}^{n} A_i}$$; **Equation 24.**

Table 3. Composite Damage Score = $(w_1 \cdot N_1) + (w_2 \cdot N_2) + \cdots + (w_n \cdot N_n)$.

Criteria	D	F	S	I	RCS	JR
D	(1, 1, 1)	(1/3, 1/2, 1)	(1/2, 1, 3/2)	(1/2, 1, 3/2)	(1/3, 1/2, 1)	(1, 2, 3)
F	(1, 2, 3)	(1, 1, 1)	(1/2, 1, 3/2)	(1/3, 1/2, 1)	(1/2, 1, 3/2)	(1, 2, 3)
S	(2/3, 1, 3/2)	(2/3, 1, 3/2)	(1, 1, 1)	(1/3, 1/2, 1)	(1/2, 1, 3/2)	(1, 2, 3)
I	(2/3, 1, 3/2)	(1, 2, 3)	(1, 2, 3)	(1, 1, 1)	(1/3, 1/2, 1)	(1, 2, 3)
RCS	(1, 2, 3)	(2/3, 1, 3/2)	(2/3, 1, 3/2)	(1, 2, 3)	(1, 1, 1)	(1, 2, 3)
JR	(1/3, 1/2, 1)	(1/3, 1/2, 1)	(1/3, 1/2, 1)	(1/3, 1/2, 1)	(1/3, 1/2, 1)	(1, 1, 1)

A fourth evaluation , based on Best-Worst Method (BWM), was likewise applied to evaluate the effectiveness of the EW system for three different scenarios: *FID* 896, *FID* 966, and *FID* 1056 as set of *n* criteria for the maximum absolute difference to be minimized (established in Equation 25) subject to weight of the best , and then worst, criterion (outlined in Equation 25) ; ensuring that the weights are normalized with a total distribution among all criteria equal to 1 (or 100%) (as confirmed in Equation 26) and non-negatives (Equation 27) hence guaranteeing validity and consistency:

$$\min_{\xi, w_i} \xi$$; **Equation 25.** $$\left|w_B - a_{Bj} \cdot w_j\right| \le \xi\ \forall j \qquad \left|w_j - a_{jW} \cdot w_W\right| \le \xi\ \forall j$$

; **Equation 26.** $$\sum_{i=1}^{n} w_j = 1$$

$$w_i \ge 0\ \forall i$$; **Equation 27.**

From the current literature, the method involves determining the most and least important criteria and then comparing these criteria against all others; for this analysis, the criteria considered were 3D Distance (C_1), Frequency Hopping (C_2), and Signal Strength (C_3); the 3D Distance (C_1) was identified as the most important criterion, and Signal Strength (C_3) as the least important.

The pairwise comparison vectors were established: the Best-to-Others vector (*BO*) with values, a_{B1} = 1, a_{B2} = 4, a_{B2} = 4, and a_{B3} = 6, and the Others-to-Worst vector (*OW*) with values a_{1W} = 6, a_{2W} = 3, and a_{3W} = 1. These vectors formed the basis of the optimization problem to determine the weights for each criterion (w_1 for C_1, w_2 for C_2, and w_3 for C_3).

After solving the optimization problem, the weights obtained were w_1 = 0.5, w_2 = 0.3, and w_3 = 0.2. The normalized values for each criterion were multiplied by their respective weights and summed to obtain the overall score N_1 (0.4773), N_2 (0.7744) and N_3 (0.8592); furthermore, these weights were then used to calculate the composite damage scores for each *FID*: 896 (0.6187), 966 (0.5899), 1056 (0.6441).

A fifth method named ELECTRE, (ELimination Et Choix Traduisant la REalité), is applied to evaluate the effectiveness of the EW system for *FID* 896, *FID* 966, and *FID* 1056 based on criteria such as 3D Distance (C_1), Frequency Hopping (C_2), and Signal Strength (C_3). First, the decision matrix A is constructed with constructed values (seen in Equation 28), and afterwards normalized (also shown in Equation 29) resulting in: w_1 , w_2 and w_3, respectively 0.3, 0.25 and 0.45:

$$A = \begin{bmatrix} 3090.88 & 3.0976 & 85.92 \\ 4120.56 & 2.8765 & 75.34 \\ 2950.34 & 3.1234 & 88.45 \end{bmatrix}$$; **Equation 28.**

$$A_{norm} = \begin{bmatrix} 0.7501 & 0.9917 & 0.9714 \\ 1.000 & 0.9209 & 0.8518 \\ 0.7161 & 1.0000 & 1.0000 \end{bmatrix}$$; **Equation 29.**

The concordance matrix C, indicating the degree to which one alternative is at least as good as another, is computed using C_{ij} where S_{ij} is the set of criteria where alternative i is better than or equal to alternative j.

Concordance Matrix (C = 0.55), which shows the degree to which one alternative is at least as good as another, the Discordance Matrix (D = 0.0548), which highlights the degree to which one alternative is strictly worse than another, and the Outranking Matrix, which integrates the concordance and discordance relationships to rank the alternatives, ultimately indicating that *FID* 896 is the most preferred alternative, followed by *FID* 966 and *FID* 1056 as presented in Equations 30 and 31:

$$A_{weighted} = \begin{bmatrix} 0.2250 & 0.2479 & 0.4371 \\ 0.3000 & 0.2302 & 0.3833 \\ 0.2148 & 0.2500 & 0.4500 \end{bmatrix}$$; **Equation 30.**

$$C_{ij} = \frac{\sum_{k \in S_{ij}} w_k}{\sum_{k=1}^{n} w_k}$$; **Equation 31.**

3.b. TOPSIS ranking of effectiveness

In the last instance, the Technique for Order Preference by Similarity to Ideal Solution (TOPSIS) was considered: the decision matrix included criteria such as 3D Distance (C_1), Frequency Hopping (C_2), Signal Strength (C_3), Interference Level (C_4), RCS (C_5), Jamming Resistance (C_6), and Number of Frequency Hopping (C_7).

By normalizing the decision matrix and applying equal weights to each criterion, we determined the ideal and negative-ideal solutions. Calculating the separation measures and relative closeness to the ideal solution, we found that *FID* 966 (A_2) ranked highest, followed by *FID* 1056 (A_3), and finally *FID* 896 (A_1). This ranking reflects the effectiveness of each radar system across all evaluated criteria, as evidenced in the following Table 4, quantitatively allocated in Equation 32 and gradually computed from Equations 33 to 41:

Table 4. TOPSIS criteria and outcomes.

Criteria	*FID* 896	*FID* 966	*FID* 1056
3D Distance (m)	3090.88	4120.56	2950.34
Frequency Hopping (GHz)	3.0976	2.8765	3.1234
Signal Strength (dB)	85.92	75.34	88.45
Interference Level (dB)	16.68	12.45	20.56
RCS (m^2)	3.73	4.12	2.56
Jamming Resistance (unitless)	0.2244	0.3345	0.1234
Number of Frequency Hopping	1000	1500	2000

$$D = \begin{bmatrix} 3090.88 & 3.0976 & 85.92 & 16.68 & 3.73 & 0.2244 & 1000 \\ 4120.56 & 2.8765 & 75.34 & 12.45 & 4.12 & 0.3345 & 1500 \\ 2950.34 & 3.1234 & 88.45 & 20.56 & 2.56 & 0.1234 & 2000 \end{bmatrix}$$

Equation 32. Decision Matrix.

$$C_1 = \sqrt{3090.88^2 + 4120.56^2 + 2950.34^2} = \sqrt{9554450.57 + 16988094.31 + 8704504.11} = \sqrt{35247049} = 5936.61$$

Equation 33 3D Distance ($C1$).

$$r_{11} = \frac{3090.88}{5936.61} = 0.5205 \ ; \ r_{21} = \frac{4120.56}{5936.61} = 0.6942 \ ; \ r_{31} = \frac{2950.34}{5936.61} = 0.4970$$

Equation 34. Normalized values for $C1$.

$$R = \begin{bmatrix} 0.5205 & 0.5651 & 0.5981 & 0.5612 & 0.5530 & 0.5156 & 0.3578 \\ 0.6942 & 0.5250 & 0.5248 & 0.4192 & 0.6112 & 0.7693 & 0.5367 \\ 0.4970 & 0.5693 & 0.6166 & 0.6916 & 0.3797 & 0.2838 & 0.7156 \end{bmatrix}$$

Equation 35. Normalized Decision Matrix R.

$$V = \begin{bmatrix} 0.0744 & 0.0807 & 0.0854 & 0.0802 & 0.0790 & 0.0737 & 0.0511 \\ 0.0992 & 0.0750 & 0.0749 & 0.0599 & 0.0873 & 0.1099 & 0.0767 \\ 0.0710 & 0.0813 & 0.0881 & 0.0988 & 0.0542 & 0.0406 & 0.1022 \end{bmatrix}$$

Equation 36. Assumed equal weights for simplicity: $w = \frac{1}{7} \approx 0.1429$.

$$V^{+} = \left(max\ v_{ij}\right) = (0.0992, \quad 0.0813, \quad 0.0881, \quad 0.0988, \quad 0.0873, \quad 0.1099, \quad 0.1022)$$
$$V^{-} = \left(min\ v_{ij}\right) = (0.0710, \quad 0.0750, \quad 0.0749, \quad 0.0599, \quad 0.0542, \quad 0.0406, \quad 0.0511)$$

Equation 37. Ideal and Negative-Ideal Solutions.

$$S^{+} = \sqrt{(0.0744 - 0.0992)^2 + (0.0807 - 0.0813)^2 + \cdots + (0.0511 - 0.1022)^2} = 0.0707$$
$$S^{-} = \sqrt{(0.0744 - 0.0710)^2 + (0.0807 - 0.0750)^2 + \cdots + (0.0511 - 0.0511)^2} = 0.0252$$

Equation 38. Separation Measures.

$$C_1^* = \frac{S_1^-}{S_1^+ + S_1^-} = \frac{0.0252}{0.0707 + 0.0252} = 0.2625$$

Equation 39. Relative Closeness to the Ideal Solution & Ranking the Alternatives (*).

$$C_2^* = \frac{S_2^-}{S_2^+ + S_2^-} = \frac{0.0531}{0.1022 + 0.0531} = 0.3424$$

Equation. 40. Relative Closeness to the Ideal Solution & Ranking the Alternatives (*).

$$C_3^* = \frac{S_3^-}{S_3^+ + S_3^-} = \frac{0.0734}{0.1421 + 0.0734} = 0.340'$$

Equation 41. Relative Closeness to the Ideal Solution & Ranking the Alternatives (*).

3.c. TOPSIS' considerations from scaled factors

This TOPSIS refinement indicated that *FID* 966 (Alternative A_2) is the most preferred radar system, value 0.3424) followed closely by *FID* 1056, value 0.3407, (Alternative A_3), and lastly *FID* 896, value 0.2625, (Alternative A_1): this ranking reflects the relative closeness of each alternative to the ideal solution, effectively capturing the performance across all evaluated criteria as specified in Table 5:

Table 5. Benchmarking of critical points in the designated ground deterrence system.

Critical Point [FID]	3D distance [mt]	Frequency Hopping [MHz]	Signal Strength (S) [dB]	Interference (I) [dB]	RCS [m2]	JR [dB/m²]	g_{11} [mt]	g_{12} [MHz]	g_{13} [dB]	g_{14} [null]	g_{15} [dB/m²]
896	3090.88	30976	85.92	16.68	3.73	0.2244	309.088	30976	0.8592	0.191	4.472
966	4120.56	28765	75.34	12.45	4.12	0.3345	412.056	28765	0.7534	0.164	3.022
1056	2950.34	31234	88.45	20.56	2.56	0.1234	295.034	31234	0.8845	0.229	8.031

To thoroughly evaluate the Radar System's performance of the ground EW truck, five AESA-based measurements have been calculated accordingly to (**A**) set of Equations sorting out the X-47B scratches of information (referring to **Table 1**): $\boldsymbol{g_{11}}$, the 3D distance scaled by a factor, measured in meters (mt). For FID 896, 966, and 1056, the values are 309.088 mt, 412.056 mt, and 295.034 mt, respectively.

Correspondingly, these distances highlight the spatial dimensions critical for radar operations, yet the scaling factor used is arbitrary and may require further justification in future activities of the department; $\boldsymbol{g_{12}}$, representing frequency hopping, with values 30976 MHz for FID 896, 28765 MHz for FID 966, and 31234 MHz for FID 1056. This indicates the system's ability to switch frequencies rapidly, enhancing jamming resistance. Nonetheless, the assumption that the hopping function is consistent and in future, the research may oversimplify real-world scenarios; $\boldsymbol{g_{13}}$, as parameter scales for the signal strength, with values are 0.8592 dB, 0.7534 dB, and 0.8845 dB for FID 896, 966, and 1056, respectively.

At this point, the scaling factor (0.01) should be critically assessed for relevance and accuracy; $\boldsymbol{g_{14}}$, as the dimensionless parameter, more clearly, the ratio of interference to signal strength plus one.

The values, 0.191, 0.164, and 0.229 for FID 896, 966, and 1056, respectively, assume that this ratio assesses the impact of interference relative to signal strength, highlighting the radar system's resilience.

The formula used is straightforward but may need refinement to account for more complex interference dynamics with a comparative quality scale of satisfaction; $\boldsymbol{g_{15}}$, representing the ratio of interference to radar cross-section: for FID 896, 966, and 1056, the values are 4.472 dB/m^2, 3.022 dB/m^2, and 8.031 dB/m^2, respectively. This metric underscores the effectiveness of interference mitigation relative to the target's radar cross-section, though the linear relationship assumed might not capture nonlinear interactions in actual conditions; **JR** , indicating the effectiveness of jamming relative to the radar cross-section. Notwithstanding, the precise JR values highlight the relative jamming effectiveness but need to be contextualized within the operational environment for a holistic assessment as further explained.

3.d.I. Telemetry data and ECM results

The weighted sum integrates factors for three critical points into a single output, balancing and reflecting each factor's relative importance across the truck position, shown as Alpha starting from Figure 10 and the X-47B trajectory, which heads west before turning back east. Initially, these sensed UCAS data were abstracted as part of the Change of Loss during training and paired with the Change of Reward (Ran, W. et al., 2023) for aerial optimization (Pan, Nan, M., 2021). This process was benchmarked in terms of velocity updates and determined Final Global Best Position (*) and Final Global Best Score (**) here quantitively listed in Table 6 and henceforth visualized in GIS mapping, from Figure 10 to Figure 16.

Table 6. FIDs and intermediate thresholds: Temperature (Kelvin).

FID	UCAS Temperature Sensed	Number of Iterations	Target Algorithm (PSO)
FID 896	288.15	84.550283	-
	437.55	84.5506	$-8.56112687\times10^{-12}$ * 8.39323714×10^{-27} **
FID 966	513.15	84.551050	-
	480.28	102.00	1.95376808×10^{-10} * 1.9565764×10^{-23} **
FID 1056	420.00	84.55104976	-

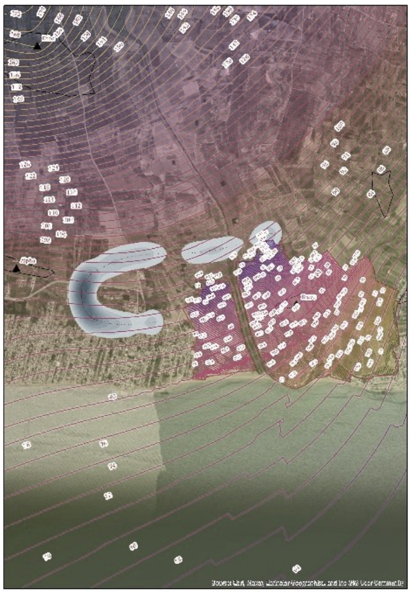
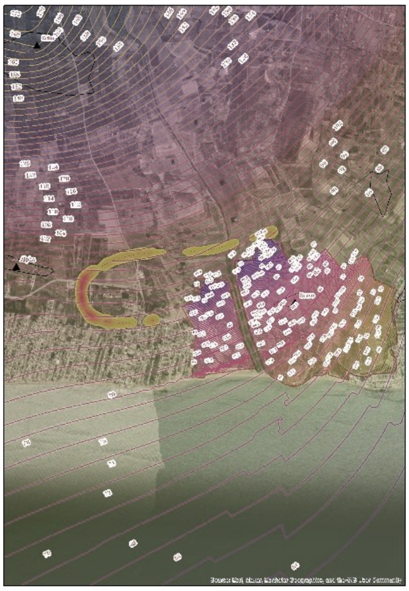
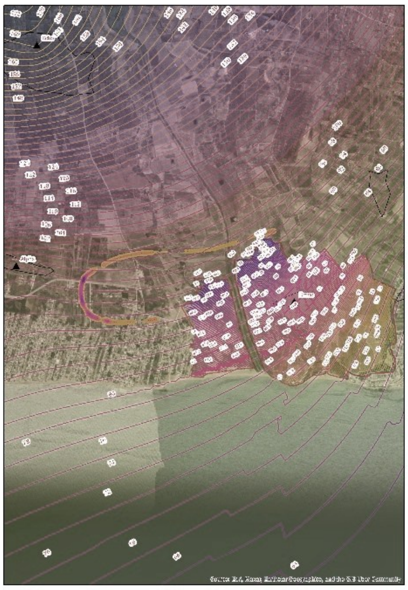

Figure 10. Path Loss Measurement Accuracy at 99.43 %, illustrating signal attenuation over varying distances.
Figure 11. Path Loss Measurement Accuracy at 99.76 %, emphasizing changes in velocity during trajectory turns.
Figure 12. Frequency Hopping Effectiveness at 99.89 %, showcasing the adaptive frequency agility.

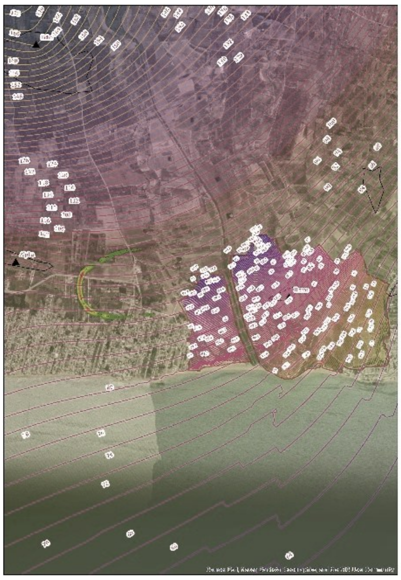
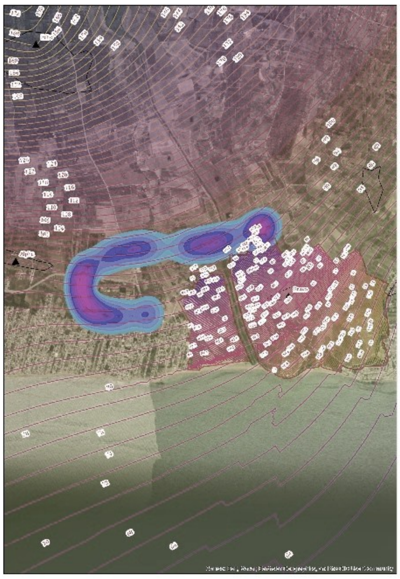
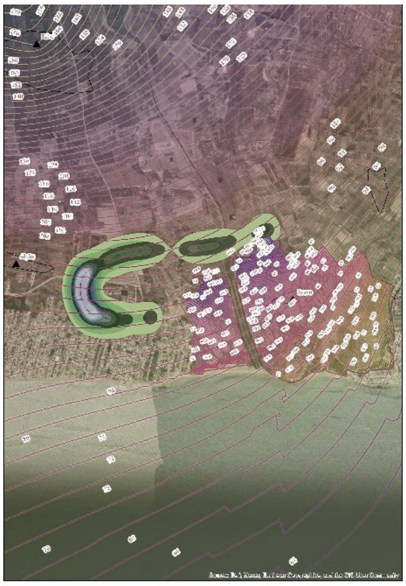

Figure 13. Critical UCAS Telemetry Data Analysis at 99,94 %.
Figure 14. 3d Distance accuracy at 90.07 %.
Figure 15. RCS 99,17 % and Savitzky–Golay 99,67 %.

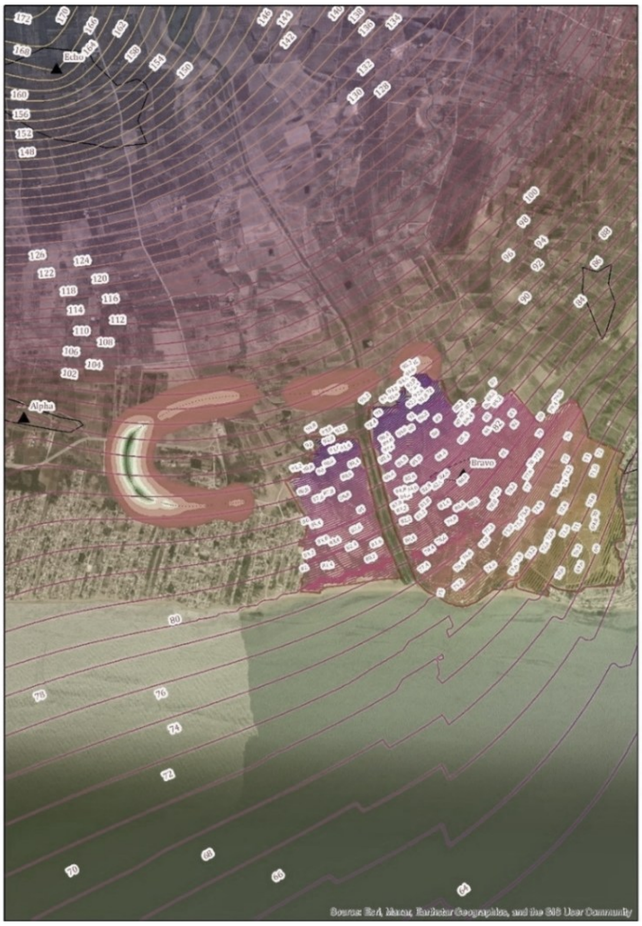

Equations 42.

$$\text{Output}_k = \sum_{i=1}^{7}\sum_{j=1}^{m}\left(L_{ij} \cdot W_i \cdot \delta_{ij}^{k}\right)$$

$$W = \begin{pmatrix} W_1 \\ \vdots \\ W_i \end{pmatrix}$$

$$L = \begin{pmatrix} L_{11} & L_{12} & \cdots & L_{1m} \\ \vdots & \vdots & \ddots & \vdots \\ L_{ii} & L_{ij} & \cdots & L_{7m} \end{pmatrix}$$

Figure 16. Weighted Sum 99.42% (Saaty T., 1988) emphasizes the significance of the PP for 7 drivers in **Equations 42.**

The weighted sum process involved multiplying each input raster layer by its corresponding weight and summing the results to produce an output raster: i) Hopping (Weight: 1); ii) Damage (Weight: 1); iii) Path Loss (Weight: 2); Velocity (Weight: 3); 3D Distance (Weight: 4); No Savitsky-Golay Section 4 Unfiltered (Weight: 5); Savitsky Filter Applied (Weight: 6).

Each criterion was carefully prepared and assigned its respective weight in the weighted sum tool within ESRI® suite. Also ensuring all raster layers were in the same coordinate system with matching cell sizes and extents is crucial for maintaining consistency and accuracy.

For kernel trajectory analysis X-47B, the Savitsky filter applied criterion holds a weak significant influence due to its refined impact on the analysis, as confirmed in Figure 17:

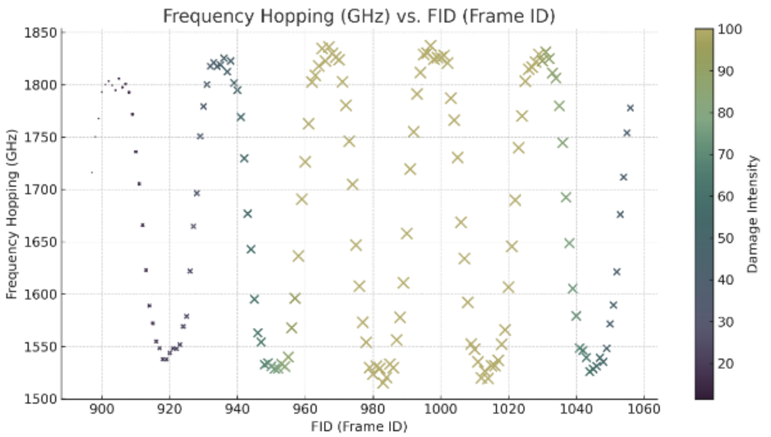

Figure 17. Profiling of X-47B damage against FIDs.

Charting trends and patterns, the profiling of UCAS Damage against Frame Identifiers (FID), we are able to observe its enhanced the statistical correlation between three frame identifiers and quantified damage intensity in the following Figure 18:

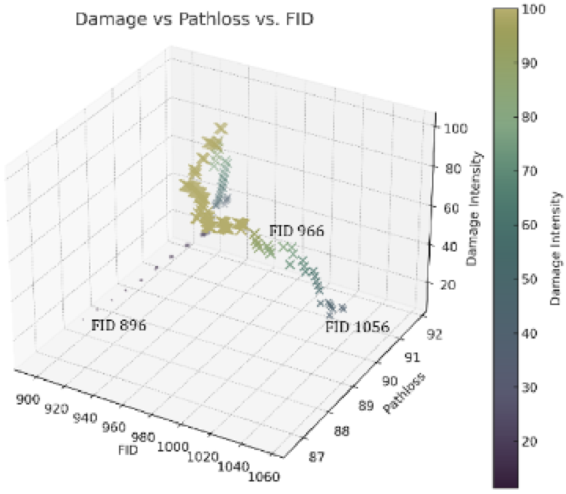

Figure 18. Profiling of X-47B damage against FIDs.

To demonstrate the variation in damage intensity as influenced by Path Loss effects across different frames. In Figure 19, the debriefing of 3D Damage in Electronic Countermeasure (ECM), provides a comprehensive visualization of damage intensity in relation to frequency hopping and frame identifiers in a three-dimensional space:

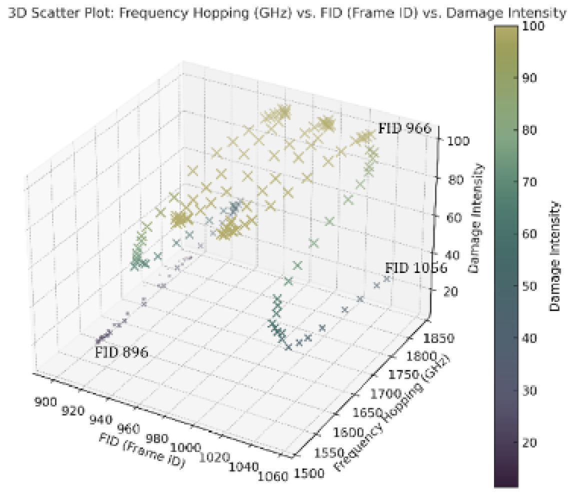

Figure 19. Path Loss Enhancement of X-47B Damage Signatures.

3.d.II. Particle Swarm Optimization

Proportionately, another critical aspect of this three-dimensional analysis is the Primary Path (PP) which is confirmed within the Consolidated Automated Support System (eCASS) for UCAS systems, along with the Systems-Theoretic Process Analysis (STPA) approach by Rising and Leveson (2018). For each FIDs, seeing 84 iterations, we adopted the Particle Swarm Optimization (PSO) method algorithm defined by its simplicity and efficiency in optimizing nonlinear functions, leveraging the social behavior of points aggregations to find optimal solutions employing the following calculation.

Explaining specifics, to solve its overall behaviour by the collective movement of multiple critical points, establishing velocity ($v_i(t)$) and position ($x_i(t)$), dynamically updated based on the inertia weight (ω), cognitive coefficient (c_1), social coefficient (c_2), and random coefficients (r_1 and r_2).

In our PSO, each potential solution to the optimization problem is represented as a “particle” as confirmed by authors Kennedy and Eberhart in their seminal 1995 paper so that two additional parameters were accounted: ϕ_1 and ϕ_2, cognitive and social, both set to 2.0 as stated in Equation 43(a).

$$v_i(t+1) = v_i(t) + \phi_1 \times (p_i(t) - x_i(t)) + \phi_2 \times (g(t) - x_i(t)) \quad ; \quad \textbf{Equation 43.}$$

$$\text{Where } x_i(t+1) = x_i(t) + v_i(t+1) \quad ; \quad \textbf{Equation 43.a.}$$

Relative to its $v_i(t)$ and $x_i(t)$, respectively velocity and position data of particle i at iteration t, we present for our critical points, as listed in Table 7:

Table 7. PSO for critical points.

	FID 896	**FID 966**	**FID 1056**
$v_i(t)$	0.097	0.687	3.787
$x_i(t)$	905.488	902.197	905.984
ω	0.5	0.6	0.7
c_1	1.5	1.3	1.1
c_2	1.5	1.3	1.1
r_1	0.7	0.5	0.6
r_2	0.3	0.4	0.2

As evidenced by author Kaveh, Ali. in 2021, we present the results in Table 7, whereby the PSO method involved resetting a portion of the particles to new, random positions at regular intervals, thus ensuring that the swarm does not converge prematurely and maintains diversity *f* as expressed in Equation 44:

$$v_i(t+1) = \omega\, v_i(t) + c_1 r_1(p_i(t) - x_i(t)) + c_2 r_2(g(t) - x_i(t)) + c_3 r_3 \frac{T}{\dot{W}} \quad ; \quad \textbf{Equation 44.}$$

A noticeable trend evidenced by Eberhart and Yuhui Shi. (2001), is its impact on the global best position, specifically of the periodic reset mechanism, 1(*) and 2(**), allocating the variable c_3, contributing to a novel domain-specific influence in terms of thrust factor also assuming as $T/\dot{W}$ for engine efficiency, as detailed in Table 8:

Table 8. Temperature values retrieved from the PSO evaluation.

	FID 896	**FID 966**	**FID 1056**
Temperature	400.0	1550.0	1500.0
$p_i(t)$*	1364.280	1279.257	1500.0
$g(t)$**	1600.0	1600.0	1600.0

3.d.III. PSO and Thrust adaptation

To contextualize the analysis of the relationship between entropy and temperature in the provided images, we expose the thrust-to-weight (T/W) ratio, a critical parameter in evaluating the performance of aircraft engines for the designated trajectory. This analysis, grounded in the performance characteristics of the Pratt & Whitney F100 jet engine, offers insights into engine efficiency and optimization, as detailed in the provided images and supported by the referenced paper by Prisacariu and Ciubotaru (2017).

Demonstrating the grounded performance of Pratt & Whitney F100 implemented in the designated UCAS X-47B, we detail in Figure 20, the supported referenced technical benchmark presented by Prisacariu and Ciubotaru in 2017 (“Henri Coandă” Air Force Academy of Braşov, Romania), albeit tailoring lowest infrared signatures consistent with stealth mode at low subsonic speeds (Krivoshchapov, A., 2019) which are appropriate for take-off along the coastal scenario of Selinunte:

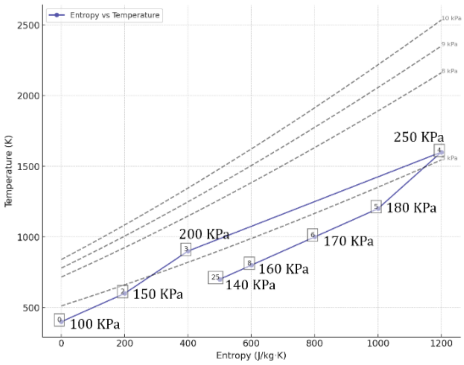

Figure 20. Correlation between entropy ($J/kg{\cdot}K$) and Temperature (K) across pressure levels (KPa).

Specifically, the polyline shows a general trend of increasing temperature with increasing entropy, indicating that higher entropy states correspond to higher temperatures within the system. This trend is consistent with the thermodynamic principles outlined by Prisacariu and Ciubotaru.

Accordingly, lower initial temperatures are retrieved from Figure 21, indicating a significant reset to a higher entropy state, leading unequivocally to a potential increase in energy or efficiency of the specific thrust (T_{sp}); as continued in Figure 22, the y-axis of the provided graph indicates the fitness values, which range from 0 to 100, color-coded from purple (low fitness) to red (high fitness), each of them representing the performance metric used in the Particle Swarm Optimization (PSO) algorithm, with higher values indicating better performance or more optimal solutions. Each icon is proportional to iteration numbers.

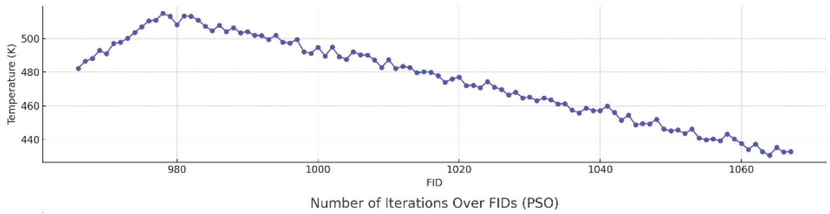

Figure 21. X-47B temperatures sensed over FIDs.

By the same token, the second image, Figure 22, provides analytical data for three FIDs: 896, 966, and 1056, (respectively 1364.280 K, 1550 K and 1279.257 K) indicating: i) along the y- axis the fitness values, which range from 0 to 100 - from purple (low fitness) to red (high fitness) - in increments of 20: each of them represents the performance metric used in the Particle Swarm Optimization (PSO) algorithm, with higher values indicating better performance or more optimal solutions.

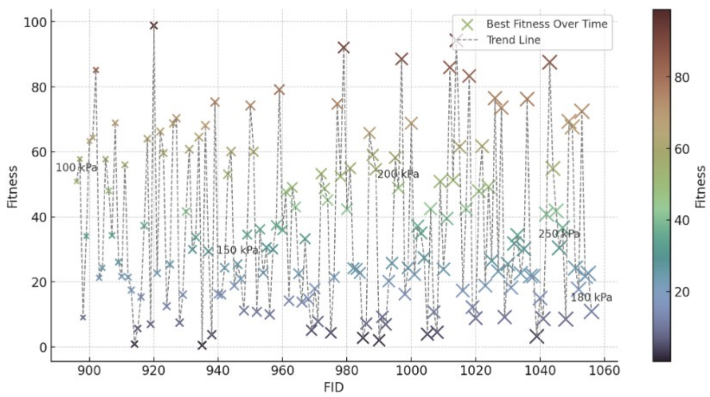

Figure 22. PSO optimization with performance values of T/W across different pressure conditions.

Nonetheless, the initial conditions, denoted as FID 896, exhibit certain limitations. The parameters include an inertia weight w of 0.5, a cognitive coefficient c_1 of 1.5, a social coefficient c_2 of 1.5, an initial velocity $v_i(t)$ of 0.097, a personal best position p_i of 1364.280, a current position ($x_i(t)$) of 905.488, and a global best position g of 1600.0. The computed subsequent velocity $v_i(t)$ is 0.472. The results match with Reward and Improvement Random Factors over iteration evaluating results of r_1 and r_2, of respectively 0.7 and 0.3.

The reward across PSOs and over iterations shows significant initial fluctuations but stabilizes as the algorithm converges towards an optimal solution. The matrix operations update the velocity vector, and the reward values indicate improvement in the objective function. Initially, these values fluctuate due to dynamic adjustments made by the PSO algorithm to find better solutions; the reward values progressively decrease, reflecting the convergence of the PSO algorithm towards the optimal resolution.

Regarding the UAV velocities, for FID 896 the velocity is 50.0 km/h, for FID 966 the velocity is 54.59 km/h, and for FID 1056 the exit velocity is 53.22 km/h.

3.d.IV. AESA vulnerability: T/R-module in heat transfer disruption

While these PSOs parameters provide a theoretically robust starting point, they may yet require considering the intrinsic complexity and variability of inherent AESA electronics, as well as the completeness of this methodology review.

To replicate the power performance graph of a GaN T/R-module front-end at 11 GHz, plotted in Figure 23, occurred within Loss-Reward Random Factors, the input power range was defined from 0 to 20 dBm and approximated the corresponding output power, gain, and PAE values using logarithmic functions based on visual data from the original graph.

The output power was calculated using the function 25 + 20 × log 10 (input power + 1), while the gain was determined with 5 + 15 × log 10 (input power + 1).

The Power Added Efficiency (PAE) was estimated as $5 + \frac{19 \times log_{10}(input\ power\ +1)}{input\ power\ +1}$; in addition, using these functions, the graph with input power, on the x-axis, and the calculated values for output power, gain, and PAE on the y-axis have been computed and plotted. The resulting benchmark provided a clear representation of how the output power, gain, and PAE varied with input power, accurately reflecting the performance characteristics of the GaN T/R-module in contrast to the jamming.

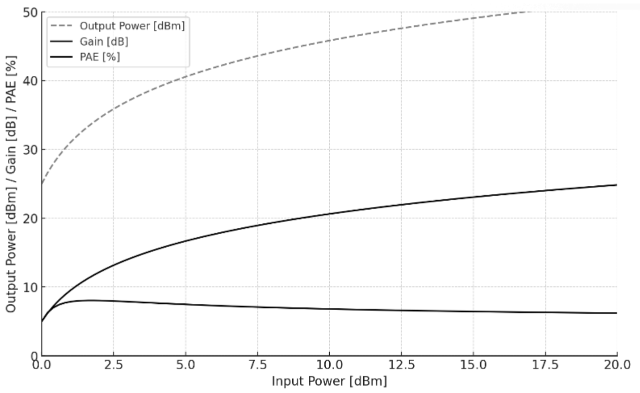

Figure 23. GaN T/R module front-end at 11 GHz.

The results in Equation 44 illustrate how the Rayleigh number (Ra) varies with the characteristic length (L) of the T/R module, providing both a visual and interpretative summary: i) the X-axis represents the characteristic length in meters, ranging from 2 mm to 10 mm, while ii) the Y-axis denotes the Rayleigh number, a crucial measure of natural convection in the system. As the characteristic length increases, the Rayleigh number rises exponentially, indicating that larger T/R modules promote greater natural convection and enhance heat transfer.

$$R_{al} = \frac{g\beta\ (T_s - T_{infinite})L^3 Pr}{v^2} \quad ; \quad \textbf{Equation 44}.$$

Assuming typical values: $g = 9.81\ m/s^2, \beta = 2.1 \times 10^{-4} K^{-1}, T_s - T_{infinite} = 50\ K, L = 0.1\ m, Pr = 0.71$, and $v = 1.5\ \times 10^{-5} m/s^2$, the Rayleigh number is $\approx\ 1.31\ \times 10^6$.

In smaller lengths (2-4 mm), the Rayleigh number is low, suggesting that heat transfer is primarily conductive with minimal natural convection. Conversely, in larger lengths (6-10 mm), the Rayleigh number significantly increases, demonstrating that natural convection becomes dominant and improves cooling efficiency. This observation is crucial for designing AESA radar cooling systems, especially when considering electronic disturbances, e.g. Variable Gain Phase Oscillator (VGPO) and Range Gate Pull-Off (RGPO).

The characteristic parameters impacting the Rayleigh number include gravity (g), thermal expansion coefficient (β), temperature difference between the surface and ambient (T_s - T_∞), characteristic length (L), Prandtl number (Pr), and kinematic viscosity (ν). The Rayleigh number formula is confirmed by authors Park, J. et al. (2021) and Gryglewski, D. et al. (2016).

3.d.IV.a. AESA and Jamming Resistance

The calculated value for the Mean Specific Damage (DMS) for the jamming attack (as confirmed in Figure 24) is -49.38, representing the combined average impact of VGPO and RGPO disturbances on the thermal performance of the AESA radar. This negative value indicates a significant reduction in cooling efficiency, raising concerns about the robustness of the current thermal management system.

Firstly, the Damage with Jamming Resistance (DRJ) value is ranked -24.48, which, despite accounting for jamming resistance, still reflects a substantial negative impact; this suggests that existing jamming resistance measures are only partially effective and insufficient to fully mitigate the effects of VGPO and RGPO disturbances.

In second instance, the Composite Specific Damage (DCS) value of -23.72 integrates the impacts of disturbances and jamming resistance, indicating an overall high level of damage to the AESA radar's performance. To define a final trend, we consider that the persistent negative values across DMS, DRJ, and DCS highlight the significant vulnerability of the system to these disturbances.

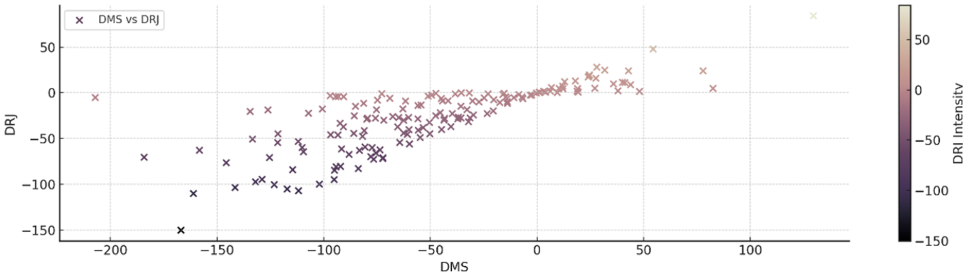

Figure 24. DMS vs DRJ.

To enhance collectively the performance of the AESA radar, it is technologically imperative to develop and implement more effective measures to reduce the impact of VGPO and RGPO disturbances; the results are crucial for applications ranging from industrial processes to advanced computing systems, where maintaining optimal thermal conditions is sensitive information.

Specifically, the correlation heatmap, generated the relationships between key factors affecting the AESA radar's performance: the correlations between VGPO and RGPO impacts are very low, indicating that these disturbances operate independently and complicate the mitigation strategy as each disturbance must be addressed separately.

Altogether, the correlation between VGPO impact and jamming resistance is also extremely low, suggesting that current jamming resistance measures do not significantly mitigate VGPO disturbances, highlighting a critical gap in the system's defence mechanisms.

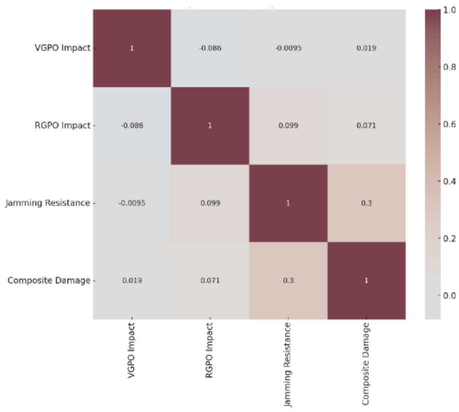

Figure 25. Correlation heatmap of EW factors impacting AESA performance.

The weak correlation between RGPO impact and jamming resistance indicates the limited effectiveness of jamming resistance measures against RGPO impacts. Although increased jamming resistance can reduce overall composite damage, the current measures are not sufficiently impactful to prevent significant performance degradation; the Figure 25 evidence such low correlations between VGPO and RGPO impacts with composite damage suggest that while their direct contributions are minimal, their cumulative effects pose significant risks to system performance.

3.d.V. MCDA retrieved from eigenvector refinement: modulation rate (γ) and interference

After range pulse compression in the time domain was considered, a Constant False Alarm Rate (CA-CFAR) detection was lastly performed, performed in Tables 9-12, on the compressed echo signal to estimate the target X-47B range accounting A_i for the echo signal i, R_i for the range of the target i, $a_r\ (t)$, the range window function, $f_{r,}$ frequency, B, bandwidth, gamma as modulation rate and c, speed of light, aggregated in terms of pairwise criterion, one by one, as aggregated in Table 9, normalized in Table 10, weighted in Table 11 and lastly fuzzified in Table 12:

Table 9. Example Pairwise Comparison Matrix for Criteria.

$$\begin{pmatrix} 1 & 1/3 & 1/2 & 1 & 1/3 & 1/5 & 1/7 \\ 3 & 1 & 3 & 1/2 & 1 & 1/3 & 1/5 \\ 2 & 1/3 & 1 & 3 & 1/2 & 1 & 1/3 \\ 1 & 2 & 1/3 & 1 & 3 & 1/2 & 1 \\ 3 & 1 & 2 & 1/3 & 1 & 3 & 1/2 \\ 5 & 3 & 1 & 2 & 1/3 & 1 & 3 \\ 7 & 5 & 3 & 1 & 2 & 1 & 1 \end{pmatrix}$$

Table 10. Normalized Matrix and Weights.

$$\begin{pmatrix} 0.05 & 0.03 & 0.07 \\ 0.15 & 0.09 & 0.13 \\ 0.20 & 0.14 & 0.18 \\ 0.10 & 0.13 & 0.11 \\ 0.25 & 0.31 & 0.21 \\ 0.15 & 0.19 & 0.16 \\ 0.10 & 0.11 & 0.14 \end{pmatrix}$$

Table 11. Weights (Eigenvector).

$$\begin{pmatrix} 0.10 \\ 0.11 \\ 0.14 \\ 0.13 \\ 0.21 \\ 0.16 \\ 0.15 \end{pmatrix}$$

Table 12. Results *Fuzzy AHP.

FID	AHP	AHP*	BWM	ELECTRE	TOPSIS
896	0.4293	0.4341	0.7187	1	3
966	0.4892	0.4845	0.6899	2	1
1056	0.3815	0.3814	0.7441	3	2

To match the maximization of the signal-to-noise ratio, the variables from the filter response for signal *r (t)*. Each method provides unique insights, contributing to a well-rounded assessment of the radar system's performance, numerically minimized and, hence, *defuzzified*, concluding with the fuzzy synthetic extents 0.75 from $\tilde{A}_{12} = (\frac{1}{3}, \frac{1}{2}, \frac{2}{3})$.

3.d.VI. SINR weighted in Fuzzy AHP triangular number and pairwise comparison

A consistent pattern, is validated in Tables 14-16, whereby the process of weighting SINR (Signal-to-Interference-plus-Noise Ratio) using Fuzzy AHP (Analytic Hierarchy Process) with triangular numbers and pairwise comparisons, detailed in Table 13, enhanced to solve the inherent uncertainty and vagueness of the trajectory, seen in Table 14 for Best-to-Others (BO) vs Others-to-Worst (OW), and lastly estimated, Table 15, characterizing the estimation by three parameters: the lower limit (a_1), the most likely value (a_2), and the upper limit (a_3):

Table 13. Fuzzy AHP triangular number and pairwise.

$$\begin{pmatrix} (1,1,1) & (2,3,4) & (4,5,6) & (6,7,8) \\ \left(\frac{1}{4},\frac{1}{3},\frac{1}{2}\right) & (1,1,1) & (2,3,4) & (4,5,6) \\ \left(\frac{1}{6},\frac{1}{5},\frac{1}{4}\right) & \left(\frac{1}{4},\frac{1}{3},\frac{1}{2}\right) & (1,1,1) & (2,3,4) \\ \left(\frac{1}{8},\frac{1}{7},\frac{1}{6}\right) & \left(\frac{1}{6},\frac{1}{5},\frac{1}{4}\right) & \left(\frac{1}{4},\frac{1}{3},\frac{1}{2}\right) & (1,1,1) \end{pmatrix};$$

Table 14. BO vs OW.

$(1\ \ 4\ \ 6\ \ 8)$ **(BO)**

$(8\ \ 4\ \ 2\ \ 1)$ **(OW)**

Table 15. Range estimation.

$$\begin{pmatrix} 85.92 & 16.68 & 20 & 0.5 \\ 75.34 & 12.45 & 25 & 0.6 \\ 88.45 & 20.56 & 15 & 0.4 \end{pmatrix}$$

As detailed, we accounted as AHP weights $w_1 = 0.5$; $w_2 = 0.2$; $w_3 = 0.1$, weighted S_i signal is equivalent to: $S_i(t)_{weighted} = 0.5 \cdot S_i\,(85.92) + 0.2 \cdot S_i(16.68) + 0.2 \cdot S_i(20) + 0.1 \cdot S_i(0.5)$ computed in **Equation 45**.

To better qualify the extent of Table 16, regular checks and periodic verification of secondary and tertiary criteria occurring at certain critical points, the formulated pairwise comparison matrix, has been raised via triangular numbers $\left(a_{ij}^L, a_{ij}^M, a_{ij}^U\right)$, completing the status of each row and column criterion.

Table 16. Fuzzy Synthetic extent.

Criteria	***R***	$\boldsymbol{\theta_{el}}$	$\boldsymbol{\theta_{azi}}$	***A***	***N***
R	(1, 1, 1)	(2/3, 1, 3/2)	(2, 3, 4)	(1/3, 1/2, 2/3)	(3, 4, 5)
θ_{el}	(2/3, 1, 3/2)	(1, 1, 1)	(1/2, 2/3, 1)	(3, 4, 5)	(2, 3, 4)
θ_{azi}	(1/4, 1/3, 1/2)	(1, 3/2, 2)	(1, 1, 1)	(2, 3, 4)	(1/3, 1/2, 2/3)
A	(3/2, 2, 5/2)	(1/5, 1/4, 1/3)	(1/3, 1/2, 2/3)	(1, 1, 1)	(2, 3, 4)
N	(1/5, 1/4, 1/3)	(1/4, 1/3, 1/2)	(3, 4, 5)	(1/2, 2/3, 1)	(1, 1, 1)

To support the overall analysis's accuracy beforehand manually computed, the defuzzification is equivalent for $\tilde{A}_{12}$ to 1.056 while $\tilde{A}_{13} \approx 3$.

Long-interval monitoring of backup and reserve criteria, like hopping and damage, ensures the data is ready for integration when needed; for high-priority weights, such as the No Savitsky-Golay section four unfiltered and the Savitsky filter applied, minimal but consistent monitoring is vital to ensure their availability and accuracy; to conclude, by computing iterated series of trajectories, a robust degree of consistency is consented, with regard of verification of all criteria layers noised via unbiased CRLB *R* estimators given by VAR $(\hat{R}) \geq \frac{\mathrm{I}}{\mathbf{I}(\theta)}$ whose Fisher Information Matrix (FIM) is determined by *r (t)*.

3.d.VII. Cramer-Rao Lower Bound and exponential refinement in radar spatial analysis

Describing the pattern documented in Figure 26 and brought by 3D spatial representation of radar data, we provide a comprehensive visualization of how radar signals varied for the three critical points; by incorporating CRLB (Cramer-Rao Lower Bound) and Exponential Smoothing accounting CRLB error bounds in variance estimator $Var\left(\hat{\theta}\right) \geq [\mathbf{I}\,(\theta)]^{-1}$ retrieving information from the Fisher Matrix.

The Y-axis indicates the elevation angle, θ_{el}, of the vertical X-47B position, while along the X-, the range measurements *(R)* is represented and for the Z-, the azimuth angle, θ_{azi}, is allocated, allowing to determining the horizontal direction of the detected trajectory α smoothed at time *t*, x_t at factor between 0 and 1 whose smoothing α factor weighted the most recent observations given by FIM. The magnitude of CRLB values is now contextualized across a two-dimensional grid as visualized in Figure 27 and summarized in Table 17. From the extracted data, we observe that the highest values, represented by the lightest colors, are concentrated around the coordinates (229, 479), (229, 480), (229, 481), (229, 457), and (402, 482). These points signify regions of maximum intensity on the heatmap, highlighting significant clusters of high values.

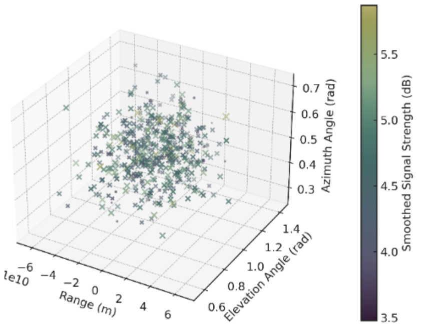

Figure 26. Cramer-Rao Lower Bound spatial intersection.

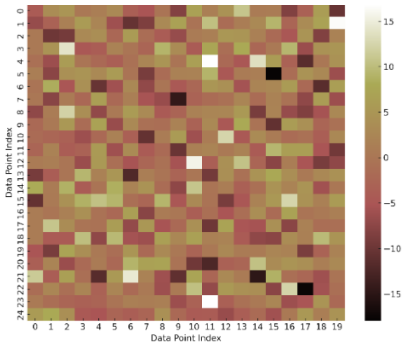

Figure 27. Heatmap of data point index from Cramer-Rao Lower.

Table 17. Heatmaps statistics.

Statistic	Mean	Median	Standard Deviation	Min	Max	25th Percentile	75th Percentile
Value	-0.000014	-0.001206	0.005612	-0.013413	0.018384	-0.002937	0.002318

The histograms presented illustrate the distribution and impact of Exponential Smoothing on various radar data parameters. Exponential Smoothing is a technique used to reduce noise and highlight significant trends in the data. By comparing the original histograms with those after smoothing, we observe that Exponential Smoothing makes the distributions more concentrated and less affected by random noise. This results in a clearer and more accurate representation of the radar data, which is crucial for improving the reliability and accuracy of radar-based measurements and estimations as portraited in Figure 28: (a) in which the top histogram displays the distribution of range estimates with Cramer-Rao Lower Bound applied; (b) whereby the top histogram shows the distribution of elevation angles in the radar data, indicating a reduction in random variability; (c) for determining the horizontal direction of detected objects; (d) characterized by the top histogram which presents the distribution of signal strengths in the radar data.

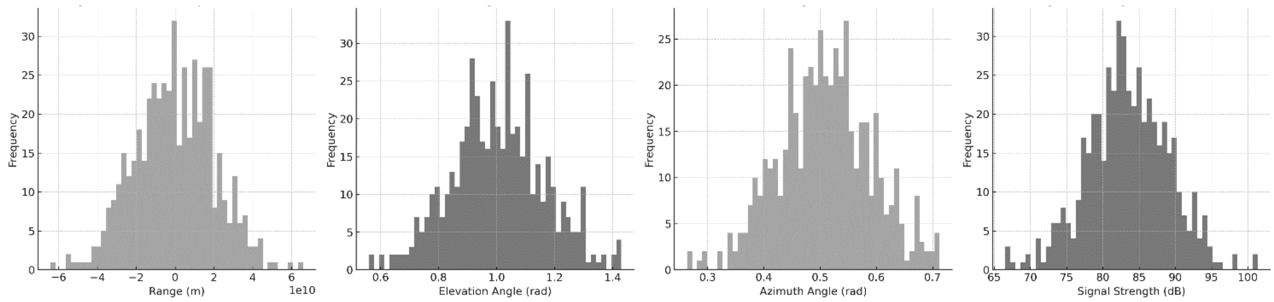

Figure 28. (a) Impact; **(b)** Elevation Angle Distribution; **(c)** Azimuth Angle Distribution; **(d)** Signal Distribution.

4. Discussion from the Methodology Review : identifying and mitigating biases in MCDA

This examination employs a novel aggregate approach, never before applied to the UCAS X-47B, to evaluate the effectiveness of EW countermeasures in the context of the Selinunte Heritage Park with the application of multiple MCDA methodologies currently implemented in the engineering industry.

In turn, the integration of advanced radar technologies, such as 3D AESA, frequency hopping, and sophisticated jamming resistance, underscores the necessity of advanced technological GIS/EW solutions to protect sensitive cultural heritage sites from modern electronic threats.

Specifically, a key and novel finding is the demonstrated utility of the TOPSIS method in ranking radar system performance across multiple criteria, which highlights its effectiveness in complex decision-making scenarios. The results, which position FID 966 and FID 1056 as the top performers, emphasize the importance of advanced signal processing and interference mitigation in EW operations. This prioritization aligns with the need for resilient systems capable of maintaining operational superiority in dynamic and contested environments.

To support the initial eCASS hypothesis, the framework also critically identifies vulnerabilities within the AESA radar system, particularly to jamming techniques such as VGPO and RGPO disturbances. The significant impact of these disturbances on thermal performance and the calculated Rayleigh number highlights the pressing need for enhanced thermal management systems; the review's findings suggest that current cooling mechanisms are inadequate, pointing to an area requiring urgent attention to prevent performance degradation under electronic attack.

Making comparisons with the iterative methodology, weighted sums and velocity updates have provided a dynamic framework for real-time adjustments, reflecting the adaptive nature of effective EW strategies. This approach allows for continuous optimization in response to evolving threats, which is crucial for maintaining an edge in EW deterrence.

Despite the strengths of the Methodology Review, there are still areas eligible for improvement, e.g. the weighting and normalization processes within the MCDA methodologies will benefit in future from further refinement to better account for the unpredictability of EW engagements.

5. Discussion and Conclusion: holistic communities and preserving heritage scenarios

This Methodology Review demonstrates the application of a comprehensive Multi-Criteria Decision Analysis (MCDA) approach to enhance Electronic Warfare (EW) countermeasures, specifically evaluating the UCAS X-47B's performance in the context of cultural heritage protection at the Selinunte Heritage Park. By employing methodologies such as AHP, ANP, Fuzzy AHP, BWM, ELECTRE, and TOPSIS, the research provides a multifaceted evaluation of key performance factors affecting EW systems, highlighting the crucial role of advanced radar technologies like 3D AESA and frequency hopping in safeguarding sensitive sites from modern electronic threats.

The findings reveal that the integration of sophisticated signal processing and interference mitigation techniques is essential for maintaining operational superiority in dynamic environments. Notably, the TOPSIS method proved effective in ranking radar systems, with FID 966 and FID 1056 identified as top performers, emphasizing the importance of resilient systems in contested scenarios.

Nonetheless, the study also uncovers vulnerabilities within the AESA radar system, particularly concerning susceptibility to jamming techniques such as VGPO and RGPO disturbances. These findings underscore the urgent need for enhanced thermal management systems to prevent performance degradation under electronic attack, suggesting that current cooling mechanisms might be insufficient.

Future research should delve deeper into the dynamic interactions between EW technologies and heritage protection frameworks, exploring how these advanced systems can be integrated without compromising the preservation of cultural assets. This interdisciplinary approach has the potential to foster holistic solutions that balance technological advancement with cultural conservation.

Overall, this study contributes valuable insights into the field of EW and heritage conservation, providing a foundational framework for future developments and innovations in both military and cultural preservation contexts. By addressing both the technological and cultural dimensions of EW, this review establishes a path for further exploration and application of advanced EW strategies in protected landscapes.

By demonstrating that the periodic reset mechanism might be a powerful enhancement to the standard Particle Swarm Optimization (PSO) algorithm, we, by periodically resetting particles, assume that the swarm of critical points could maintain its ability to explore new areas of the search space, thereby increasing the likelihood of finding the global optimum. Despite the additional computational cost and the need for careful parameter tuning, the benefits of periodic resets in terms of improved UCAS optimization performance make it a valuable strategy in swarm intelligence and optimization. Enhanced exploration by periodically resetting particles helps the PSO maintain a higher level of exploration, preventing premature convergence and increasing the chances of finding the global optimum. Maintaining diversity within the swarm ensures that different regions of the search space are explored, leading to better optimization results as the swarm is less likely to get trapped in local optima.

Lastly, introducing periodic resets can increase the computational load due to the generation of new random positions and velocities. The effectiveness of the reset mechanism depends on parameters such as the reset interval (TTT) and the fraction of particles to reset, which need careful tuning for different optimization problems. If the reset interval is too short or the fraction of reset particles is too high, it may disrupt the convergence process and lead to inefficiency.

Acknowledgement

This research did not receive any specific grant from funding agencies in the public, commercial, or not-for-profit sectors. It was initiated through a joint agreement between the Department of Architecture at the Hamdullah Emin Paşa Campus of Alanya University and the Department for Training and Internationalization of the *Ordine degli Architetti, Pianificatori, Paesaggisti e Conservatori* of Naples and its Province, Italy, recognized under Royal Decree No. 2537 of October 23, 1925.

All images included in this work were created by the primary author. Acknowledgements are extended to all peers who contributed to the development of an accessible research methodology, with special thanks to the two anonymous reviewers for their insightful evaluation of the proposed framework.

Conflict of Interests

The authors declare no conflict of interest. The numerical results and their processing do not imply any responsibility in terms of the design, collection, or interpretation of data, but are exclusively intended to demonstrate appropriate and well-calibrated methodologies in support of *Valutazione di Impatto Ambientale* (VIA, Environmental Impact Assessment) and *Valutazione Ambientale Strategica* (VAS, Strategic Environmental Assessment). The research endorses the reintroduction of historically coherent and ecologically compatible components of infrastructures, promoting a sustainable approach to land use, and adopts data extraction methods that exclude animal experimentation and avoid environmentally invasive procedures, in full compliance with the rigorous Italian legislation on landscape protection.

Ethics statements

This study was conducted in accordance with the principles outlined in the European Code of Ethics for Scientific Research and adheres to the Declaration of Helsinki (2013). It received approval from the appropriate Institutional Review Board.

The research posed no harm or risk to participants, and all data collected were used solely to investigate the built environment in relation to Heritage Architecture. All data are strictly unclassified and have been made publicly available without any violation of copyright or intellectual property rights.

For any inquiries or concerns regarding the study, please refer to the official contact details of the hosting university.

References

Alharasees, Omar, and Utku Kale. (2024). Evaluation of Air Transport Projects Development by AHP. In *Green Approaches in Sustainable Aviation*, a cura di T. Hikmet Karakoc, Raj Das, Ismail Ekmekci, Alper Dalkiran, e Ali Haydar Ercan, 55–64. Sustainable Aviation. Cham: Springer Nature Switzerland. https://doi.org/10.1007/978-3-031-33118-3_8.

Balcerzak, Tomasz, and Małgorzata Sieradzka. (2022). Polish Criminal Liability of the UAV Operator in Connection with the Unauthorized Flight in Operations Area of Fire Services in the Context of the Possibility of the U-Space Using. *Journal of Intelligent & Robotic Systems* 106, fasc. 1 : 25. https://doi.org/10.1007/s10846-022-01727-9.

Barakat, Sultan. (2021). Necessary Conditions for Integrated Approaches to the Post-Conflict Recovery of Cultural Heritage in the Arab World. *International Journal of Heritage Studies* 27, n. 5: 433–48. https://doi.org/10.1080/13527258.2020.1799061.

Belal, A., e E. Shcherbina. (2019). Heritage in Post-War Period Challenges and Solutions. *IFAC-PapersOnLine* 52, n. 25: 252–57. https://doi.org/10.1016/j.ifacol.2019.12.491.

Borja, Díaz Ariño. (2021). Epigraphy and Collective Memory: Cicero and the War Booty Inscriptions. *Classical Philology* 116, fasc. 3: 435–45. https://doi.org/10.1086/714433.

Bozzano, Matteo, Domenico Sguerso, Paolo Zatelli, Davide Zendri, and Angelo Besana. (2024). Accuracy Evaluation for Plan-Reliefs and Historical Maps Created during WWI in Northern Italy. *ISPRS International Journal of Geo-Information* 13, fasc. 3 : 101. https://doi.org/10.3390/ijgi13030101.

Brosché, J., Legnér, M., Kreutz, J., & Ijla, A. (2016). Heritage under attack: motives for targeting cultural property during armed conflict. *International Journal of Heritage Studies*, *23*(3), 248–260. https://doi.org/10.1080/13527258.2016.1261918.

Chang, Da-Yong. (1996). Applications of the Extent Analysis Method on Fuzzy AHP. *European Journal of Operational Research* 95, fasc. 3: 649–55. https://doi.org/10.1016/0377-2217(95)00300-2.

Chen, Chen-Tung, Ching-Torng Lin, and Sue-Fn Huang. (2006). A Fuzzy Approach for Supplier Evaluation and Selection in Supply Chain Management. *International Journal of Production Economics* 102, fasc. 2 : 289–301. https://doi.org/10.1016/j.ijpe.2005.03.009.

Chetverikov, Borys, Luybov Babiy, Szymon Oryński, and Sebastian Różycki. (2024). Methods for Designating Protective Zones of Historical and Cultural Purpose Using Non-Invasive Methods—Two Case Studies for Ukraine and Poland. *Remote Sensing* 16, fasc. 13 : 2330. https://doi.org/10.3390/rs16132330.

Chetverikov, Borys, Volodymyr Hlotov, and Krzysztof Bakuła. (2024). Clarification of the Boundaries of Lands of Historical and Cultural Heritage and Determination of Their Protection Zones by Remote Sensing Methods. *Land* 13, fasc. 7 : 923. https://doi.org/10.3390/land13070923.

Chizzoniti, Domenico Giuseppe, and Tommaso Lolli. (2023). Urban Morphology, Identity, Heritage, and Reconstruction Processes in Middle East Post-War Scenarios: The Case of Mosul Old City. *Land* 12, fasc. 12 : 2140. https://doi.org/10.3390/land12122140.

Choi, Seungcheol, Oh-Jin Kwon, Haengrok Oh, and Dongkyoo Shin. (2020). Method for Effectiveness Assessment of Electronic Warfare Systems in Cyberspace. *Symmetry* 12, fasc. 12 : 2107. https://doi.org/10.3390/sym12122107.

Committee on Improving the Effectiveness and Efficiency of U.S. Air Force Pre-Acquisition Development Planning, Air Force Studies Boad – Division on Engineering and Physical Sciences – National Research Council. (2014). *Development Planning: A Strategic Approach to Future Air Force Capabilities*. Washington, D.C.: National Academies Press. https://doi.org/10.17226/18971.

De Souza, Leandro Peçanha, Carlos Francisco Simões Gomes, and Alexandre Pinheiro De Barros. (2018). Implementation of New Hybrid AHP–TOPSIS-2N Method in Sorting and Prioritizing of an It CAPEX Project Portfolio. *International Journal of Information Technology & Decision Making* 17, fasc. 04 : 977–1005. https://doi.org/10.1142/S0219622018500207.

Di Mauro, L., Ahmad Nia, H., Capobianco, L., Polverino, S. and Coppola, A. (2024). Context-responsive decision-making to enhance Multilateral Agreements in Core Principles Cultural Heritage Preservation. In Innovative Approaches to Cultural Heritage and Sustainable Urban Development: Integrating Tradition and Modernity (Integrating Tradition and Modernity, Chapter 21). Cinius Yayınları. https://doi.org/10.38027/N21ICCAUA2024EN0001.

Eberhart and Yuhui Shi. (2001). Particle swarm optimization: developments, applications and resources. In *Proceedings of the 2001 Congress on Evolutionary Computation (IEEE Cat. No.01TH8546)*, 1:81–86. Seoul, South Korea: IEEE. https://doi.org/10.1109/CEC.2001.934374.

Feis, Herbert. (2016). 5. On War Booty and Restitution. *Between War and Peace*, Princeton: Princeton University Press, 1960, pp. 336-337. https://doi.org/10.1515/9781400876761-047.

Gryglewski, Daniel, Dawid Rosolowski, Wojciech Wojtasiak, Marcin Goralczyk, and Wojciech Gwarek. (2016). A 10W GaN based X-band T/R module for AESA. In *2016 21st International Conference on Microwave, Radar and Wireless Communications (MIKON)*, 1–4. Krakow, Poland: IEEE. https://doi.org/10.1109/MIKON.2016.7491978.

Hamurcu, Mustafa, and Tamer Eren. (2020). Selection of Unmanned Aerial Vehicles by Using Multicriteria Decision-Making for Defence. *Journal of Mathematics* 2020 : 1–11. https://doi.org/10.1155/2020/4308756.

"Henri Coandă" Air Force Academy of Braşov, Romania, Vasile Prisacariu, Alexandru Ciubotaru, and "Henri Coandă" Air Force Academy of Braşov, Romania. (2017). ASPECT REGARDING OF THE PRATT & WHITNEY F100 JET ENGINE PERFORMANCES. *SCIENTIFIC RESEARCH AND EDUCATION IN THE AIR FORCE* 19, fasc. 1 : 187–94. https://doi.org/10.19062/2247-3173.2017.19.1.20.

Hoeniger, Cathleen. (2024). The Protection of Monuments and Immoveable Works of Art from War Damage: A Comparison of Italy in World War II and Ukraine during the Russian Invasion. *Arts* 13, fasc. 2 : 65. https://doi.org/10.3390/arts13020065.

Kaveh, Ali. (2021). Particle Swarm Optimization. In *Advances in Metaheuristic Algorithms for Optimal Design of Structures*, di Ali Kaveh, 13–46. Cham: Springer International Publishing. https://doi.org/10.1007/978-3-030-59392-6_2.

Kennedy, Hugh L. (2020). Improving the Frequency Response of Savitzky-Golay Filters via Colored-Noise Models. *Digital Signal Processing* 102 : 102743. https://doi.org/10.1016/j.dsp.2020.102743.

Kennedy, Hugh Lachlan. (2023). A Versatile Procedure for the Design of FIR and IIR Filters With Phase-Derivative Estimation Examples and Electronic-Warfare Applications. https://doi.org/10.13140/RG.2.2.21755.28961.

Kennedy, J., and R. Eberhart. (1995). Particle swarm optimization. In *Proceedings of ICNN'95 - International Conference on Neural Networks*, 4:1942–48. Perth, WA, Australia: IEEE. https://doi.org/10.1109/ICNN.1995.488968.

Khalaf, Roha W. (2017). A Viewpoint on the Reconstruction of Destroyed UNESCO Cultural World Heritage Sites. *International Journal of Heritage Studies* 23, n. 3: 261–74. https://doi.org/10.1080/13527258.2016.1269239.

Kong, Xiangxiong, and Ronny Garrett Hucks. (2023). Preserving Our Heritage: A Photogrammetry-Based Digital Twin Framework for Monitoring Deteriorations of Historic Structures. *Automation in Construction* 152 : 104928. https://doi.org/10.1016/j.autcon.2023.104928.

Krivoshchapov, A. A. (2019). Experimental Studies of X-47B-Type Unmanned Aerial Vehicle in TsAGI T-102 Wind Tunnel to Assess Effectiveness of Aerodynamic Controls in Longitudinal Channel. *Russian Aeronautics* 62, fasc. 2 : 342–47. https://doi.org/10.3103/S1068799819020247.

Leijonhufvud, Gustaf, Tor Broström, Alessia Buda, Daniel Herrera, Franziska Haas, Alexandra Troi, Dagmar Exner (2021) Planning energy retrofits of historic buildings. IEA SHC Task 59. https://doi.org/10.18777/ieashc-task59-2021-0003.

Liang, Wen, Yahaya Ahmad, and Hazrina Haja Bava Mohidin. (2023). The development of the concept of architectural heritage conservation and its inspiration. *Built Heritage* 7, fasc. 1: 21. https://doi.org/10.1186/s43238-023-00103-2.

Liang, Xueping, Juan Zhao, Sachin Shetty, and Danyi Li. (2017). Towards data assurance and resilience in IoT using blockchain. In *MILCOM 2017 - 2017 IEEE Military Communications Conference (MILCOM)*, 261–66. Baltimore, MD: IEEE. https://doi.org/10.1109/MILCOM.2017.8170858.

Ling, Qing, Penghui Huang, Donghong Wang, Huajian Xu, Lingyu Wang, Xingzhao Liu, Guisheng Liao, and Yongyan Sun. (2023). Range Deception Jamming Performance Evaluation for Moving Targets in a Ground-Based Radar Network. *Electronics* 12, fasc. 7 : 1614. https://doi.org/10.3390/electronics12071614.

Loulanski, Tolina. (2006). Revising the Concept for Cultural Heritage: The Argument for a Functional Approach. *International Journal of Cultural Property* 13, n. 02. https://doi.org/10.1017/S0940739106060085.

Madrigal Manuel Pagés , José. (2018). Some Notes about Architecture, Urbanism and Economy. *Journal of Contemporary Urban Affairs* 2, fasc. 2 : 1–11. https://doi.org/10.25034/ijcua.2018.3663.

Mohammadi, Majid, and Jafar Rezaei. (2020). Bayesian Best-Worst Method: A Probabilistic Group Decision Making Model. *Omega* 96 : 102075. https://doi.org/10.1016/j.omega.2019.06.001.

Najd Deghati, Meysam, Nor Atiah Ismail, Maulan Suhardi, Mohd Yunos Mohd Yazid, and Dabbagh Niya Mahsa. (2015). Visual Preference Dimensions of Historic Urban Areas: The Determinants for Urban Heritage Conservation. *Habitat International* 49: 115–25. https://doi.org/10.1016/j.habitatint.2015.05.003.

Nia, Hourakhsh Ahmad, and Yousif Hussien Suleiman. (2017). Identity in Changing Context: Factors of losing Identity in new developed part of the city of Famagusta, North Cyprus. *Journal of Contemporary Urban Affairs* 1, fasc. 2 : 11–20. https://doi.org/10.25034/ijcua.2017.3644.

Pan, Nan, Miaohan Zhang, Yuxuan Sun, Shiyun Chen, Haishi Liu, and Xiaojue Guo. (2021). Study on Border Patrol Task Planning of Heterogeneous UAVs Group Based on Swarm Intelligence. *Science Progress* 104, fasc. 4_suppl: 003685042210947. https://doi.org/10.1177/00368504221094722.

Park, Jun Su, Dong-Jun Shin, Sung-Hwan Yim, and Sang-Hyun Kim. (2021). Evaluate the Cooling Performance of Transmit/Receive Module Cooling System in Active Electronically Scanned Array Radar. *Electronics* 10, fasc. 9 : 1044. https://doi.org/10.3390/electronics10091044.

Polverino, S. (2024). Integrating InSAR and Landsat for strategic heritage site protection: EW ground analysis and path loss in Selinunte Park. In *Innovative approaches to cultural heritage and sustainable urban development: Integrating tradition and modernity* (Edition: Integrating tradition and modernity, Chapter 12). Cinius Yayınları. http://dx.doi.org/10.38027/N12ICCAUA2024EN0070.

Proakis, J. G. and Salehi, M. (2007). *Digital Communications 5th Edition*. McGraw Hill, New York.

Rahbarianyazd, Rokhsaneh. (2017). Sustainability in Historic Urban Environments: Effect of gentrification in the process of sustainable urban revitalization. *Journal of Contemporary Urban Affairs* 1, fasc. 1 : 1–9. https://doi.org/10.25034/1761.1(1)1-9.

Ran, W.; Luo, R.; Zhang, F.; Luo, R.; Xu, Y. (2023). Research on Efficient Multiagent Reinforcement Learning for Multiple UAVs' Distributed Jamming Strategy. Electronics, 12, 3874. https://doi.org/10.3390/electronics12183874.

Richards, J., Brimblecombe, P. (2022). The transfer of heritage modelling from research to practice. *Herit Sci* **10**, 17. https://doi.org/10.1186/s40494-022-00650-4.

Rising, John M., and Nancy G. Leveson. (2018). Systems-Theoretic Process Analysis of Space Launch Vehicles. *Journal of Space Safety Engineering* 5, fasc. 3–4 : 153–83. https://doi.org/10.1016/j.jsse.2018.06.004.

Rosser, Pablo, and Seila Soler. (2024). From Oblivion to Life: The Recovery of Intangible Cultural Heritage through the Anti-Aircraft Shelters of the Spanish Civil War. *Heritage* 7, fasc. 2 : 817–28. https://doi.org/10.3390/heritage7020039.

Saaty, Thomas L. (1988) What Is the Analytic Hierarchy Process? In *Mathematical Models for Decision Support*, a cura di Gautam Mitra, Harvey J. Greenberg, Freerk A. Lootsma, Marcel J. Rijkaert, e Hans J. Zimmermann, 109–21. Berlin, Heidelberg: Springer Berlin Heidelberg. https://doi.org/10.1007/978-3-642-83555-1_5.

Schofield, John. (2009). Introduction Considering Virilio's (1994) Bunker Archeology. In *Aftermath*, di John Schofield, 1–13. New York, NY: Springer New York. https://doi.org/10.1007/978-0-387-88521-6_1.

Seidaliyeva, Ulzhalgas, Lyazzat Ilipbayeva, Kyrmyzy Taissariyeva, Nurzhigit Smailov, and Eric T. Matson. (2023). Advances and Challenges in Drone Detection and Classification Techniques: A State-of-the-Art Review. *Sensors* 24, fasc. 1 : 125. https://doi.org/10.3390/s24010125.

Selver, M A, M Secmen, and E Y Zoral. (2018). Savitzky-Golay filtering for Scattered Signal De-noising. *Journal of Physics: Conference Series* 1141 : 012151. https://doi.org/10.1088/1742-6596/1141/1/012151.

Smith, Ryan N., Dario Cazzaro, Luca Invernizzi, Giacomo Marani, Song K. Choi, and Monique Chyba. (2011). A Geometric Approach to Trajectory Design for an Autonomous Underwater Vehicle: Surveying the Bulbous Bow of a Ship. *Acta Applicandae Mathematicae* 115, fasc. 2: 209–32. https://doi.org/10.1007/s10440-011-9616-8.

Sijabat, J P, e T Indriyanto. (2021). Radar Cross Section Analysis of Unmanned Combat Aerial Vehicle (UCAV) using FEKO Software. *AVIA* 2, fasc. 2. https://doi.org/10.47355/avia.v2i2.19.

Sozinov, P.A., G.I. Andreev, V.A. Tikhomirov, and M.E. Zamarin. (2023). The concept of protecting a multifunctional aircraft with an electronic warfare system. *Radioengineering* 10. https://doi.org/10.18127/j00338486-202310-01.

Spennemann, Dirk HR. (2020). Using KOCOA Military Terrain Analysis for the Assessment of Twentieth Century Battlefield Landscapes *Heritage* 3, no. 3: 753-781. https://doi.org/10.3390/heritage3030042.

Spennemann, D. H. R., & Poynter, C. (2019). Using 3D spatial visualisation to interpret the coverage of anti-aircraft batteries on a World War II battlefield. *Heritage, 2*(3), 2457-2479. https://doi.org/10.3390/heritage2030151.

Stone, Peter. (2022). Preface: The Blue Shield and the Protection of the World's Cultural Property – Preparing in Peace for Conflict. In *Safeguarding Cultural Property and the 1954 Hague Convention*, a cura di Emma Cunliffe e Paul Fox, 1º ed., xvii–xxii. Boydell and Brewer Limited,. https://doi.org/10.1017/9781800104273.001.

Sun, Chia-Chi. (2010). A Performance Evaluation Model by Integrating Fuzzy AHP and Fuzzy TOPSIS Methods. *Expert Systems with Applications* 37, fasc. 12 : 7745–54. https://doi.org/10.1016/j.eswa.2010.04.066.

Tarquini, Simone, and Luca Nannipieri. (2017). The 10 M-Resolution TINITALY DEM as a Trans-Disciplinary Basis for the Analysis of the Italian Territory: Current Trends and New Perspectives. *Geomorphology* 281: 108–15. https://doi.org/10.1016/j.geomorph.2016.12.022.

Taherdoost, Hamed, and Mitra Madanchian. (2023). Analytic Network Process (ANP) Method: A Comprehensive Review of Applications, Advantages, and Limitations. *Journal of Data Science and Intelligent Systems* 1, fasc. 1 : 12–18. https://doi.org/10.47852/bonviewJDSIS3202885.

Uzun, Berna, Rwiyereka Angelique Bwiza, and Dilber Uzun Ozsahin. ELimination Et Choix Traduisant La REalité (ELECTRE). (2021). In *Application of Multi-Criteria Decision Analysis in Environmental and Civil Engineering*, a cura di Dilber Uzun Ozsahin, Hüseyin Gökçekuş, Berna Uzun, e James LaMoreaux, 31–36. Professional Practice in Earth Sciences. Cham: Springer International Publishing. https://doi.org/10.1007/978-3-030-64765-0_5.

Yuan, Chengen, Dongli Ma, Yuhong Jia, and Liang Zhang. (2024). Stealth Unmanned Aerial Vehicle Penetration Efficiency Optimization Based on Radar Detection Probability Model. *Aerospace* 11, fasc. 7 : 561. https://doi.org/10.3390/aerospace11070561.

Wang, Guo Sheng, and Zong Feng Qi. (2014). AHP Effectiveness Evaluation of Electronic Warfare Command and Control System under Complex Electromagnetic Environment. *Advanced Materials Research* 989–994 : 3212–15. https://doi.org/10.4028/www.scientific.net/AMR.989-994.3212.

Wang, Ruochen, Guoxin Zhang, Xinhui Zhao, Bo Wang, and Xiaoping Ma. (2022). An Integrated Optimization Method of Wingtip Stealth/Aerodynamic Using Surrogate-Based Method. In *Proceedings of 2021 International Conference on Autonomous Unmanned Systems (ICAUS 2021)*, a cura di Meiping Wu, Yifeng Niu, Mancang Gu, e Jin Cheng, 861:348–57. Lecture Notes in Electrical Engineering. Singapore: Springer Singapore. https://doi.org/10.1007/978-981-16-9492-9_35.

Wu, Yuhan, Yabo Dong, Zeyang Shan, Xiyu Meng, Yang He, Ping Jia, and Dongming Lu. (2024). Enhancing Anomaly Detection for Cultural Heritage via Long Short-Term Memory with Attention Mechanism. *Electronics* 13, fasc. 7 : 1254. https://doi.org/10.3390/electronics13071254.

Zadeh, L. A. (1965). Fuzzy sets. Information and Control, 8(2), 338–353.

Zadeh, Lotfi A. (1994). The Role of Fuzzy Logic in Modeling, Identification and Control. *Modeling, Identification and Control: A Norwegian Research Bulletin* 15, fasc. 3 : 191–203. https://doi.org/10.4173/mic.1994.3.9.

Zaina, Federico, Paola Branduini, and Fereshteh Zavvari. (2022). Applying ICOMOS-IFLA Principles for the Conservation, Management and Reuse of a Historical Hydraulic System: The No-Ras Qanat in North-Western Iran. *Heritage* 5, fasc. 4: 3165–87. https://doi.org/10.3390/heritage5040163.

Zhang, Xixiang, Kaiqi Xiao, and Jie Gu. (2022). *Theory to Countermeasures Against New Radars*. Singapore: Springer Nature Singapore. https://doi.org/10.1007/978-981-16-6715-2.

Zou, Yifei, Li Yang, Guanlin Jing, Ruirui Zhang, Zhenzhen Xie, Huiqun Li, and Dongxiao Yu. (2024). A Survey of Fault Tolerant Consensus in Wireless Networks. *High-Confidence Computing* 4, fasc. 2 : 100202. https://doi.org/10.1016/j.hcc.2024.100202.